Revision 2

Word count: 8488 (excluding figure captions and references)

Miyake-jima Anorthite: A Lunar Crustal Material Analog

Arkadeep Roy[1], Ananya Mallik[1], Kerri Donaldson Hanna[2], Tyler J. Goepfert[3], Richard L. Hervig[3]

[1] Department of Geosciences, University of Arizona, 1040 E 4th St, Tucson, AZ 85721, USA

[2] Department of Physics, University of Central Florida, 4111 Libra Drive, Orlando, Florida, FL 32816, USA

[3] Arizona State University, School of Earth & Space Exploration, 550 E Tyler Mall, Tempe, AZ 85287-1404, USA

Corresponding author: Arkadeep Roy (arkadeeproy@arizona.edu)

Abstract: High calcic (~95% anorthite) plagioclase is the key mineral comprising the primary lunar crustal suites that cover over 60% of the Moon's surface. Pristine crystals of similar high calcic plagioclase are rare occurrences on Earth, which creates a roadblock to using terrestrial material as lunar crustal analogs. We discuss the potential of a particular megacrystic anorthite ($An_{95.51 \pm 0.31}$) occurring in the basaltic lava flows of island arc volcano in Miyake-jima, Japan as an material analog. A comprehensive analytical routine for the Miyake-jima anorthites has been performed to explore intra- and inter-crystalline heterogeneities in terms of major, minor, and trace elements. These anorthites show flat concentration gradients across core profiles for all

major elements (Si, Al, Ca, Na), minor elements (Mg, Fe), and most trace elements (La, Ce, Pm, Nd, Eu). Comparing the chemical composition of the samples with that of different lunar crustal suites like ferroan anorthosites, high-magnesium suites, and high alkali suites show that the Miyake-jima anorthites are overlapping or depleted in most minor and trace elements except for a slight enrichment in Li, Ti, Fe, Sr, Eu, Ba, and Pb. Given the low abundance of most trace elements in the Miyake-jima anorthites we can treat this sample suite as a "blank slate", which provides the opportunity to dope the crystalline matrix with the elements of interest at different levels and use them for geochemical, petrologic, and spectroscopic studies. The lack of typical magmatic zoning and overlapping elemental compositions across the different megacrysts make the Miyake-jima anorthites very well-suited as a lunar crustal material analog. Highly calcic, crystalline anorthite is shown to have unique spectral signatures from less calcic anorthite, and intermediate and sodic compositions of plagioclase feldspar as calcium and iron contents control the wavelength position and shape of the diagnostic spectral features in the thermal infrared region of the electromagnetic spectrum. Thus, near and thermal infrared spectral measurements of the Miyake-jima anorthites highlight the importance of developing chemically and mineralogically consistent terrestrial material analogs for remote sensing studies.

Keywords: *Natural anorthite megacrysts, lunar material analog, major and trace elements, near-infrared and thermal-infrared spectra*

1. Introduction

Plagioclase feldspar, specifically anorthite (An-), is the most dominant mineral in the ferroan anorthosites (FAN), which constitute the lunar highlands (Dowty et al., 1974). The highlands comprise of almost all the lunar farside and also large sections of the lunar nearside crust. The plagioclase in FAN is compositionally restricted to An_{94-98} and contains minor Fe-rich pyroxenes, which led to their FAN nomenclature (Dowty et al., 1974; McGee, 1993). Traces of olivine, silica, chromite, ilmenite, and spinel in the FAN suites have also been reported. The widespread distribution of highly anorthitic plagioclase on the Moon's surface is due to the preservation of large sections of the primary lunar crust, which is thought to have crystallized from the late magma ocean (Smith et al,. 1970; Wood et al., 1970; Walker and Hays, 1977; Warren, 1985; Shearer et al., 2006; Grove and Krawczynski, 2009). In contrast, Earth's primary crust has been expunged through recycling and secondary crust building processes (Herzberg and Rudnick, 2012; Foley et al., 2002). Although typical terrestrial anorthosite massifs have >90% modal abundance of plagioclase, these monomineralic rocks are not associated with high calcic-plagioclase. The increase in modal plagioclase is generally associated with mineral compositions becoming more labradoritic (Bowen, 1917). Smaller ophitic anorthite crystals ($An_{90–100}$) are commonly encountered in island-arcs (Arculus and Wills, 1980; Brophy, 1986), intraoceanic forearcs (Falloon and Crawford, 1991), and mid-ocean ridge basalts (Donaldson and Brown, 1977; Stakes et al., 1984) typically forming under water saturated conditions (Sisson and Grove, 1993). Therefore, there exists a dearth of naturally occurring large and pristine ~An_{95} plagioclase crystals that could be used as a potential lunar material analog for geochemical, spectroscopic, geophysical and experimental petrology studies. There have been previous attempts at developing Stillwater anorthosite as a potential lunar material analog (Salpas et al. 1983).

71 However, the anorthite content (or An# which is the molar Ca/[Ca + Na + K] ratio of
72 plagioclase) of most plagioclase from the Stillwater complex varies from $An_{69 - 83}$, which is less
73 calcic than lunar FAN, rendering them a poorly suited material analog. In addition, the Stillwater
74 anorthosites show textures of zoning and overgrowth that amplifies the intracrystalline
75 heterogeneity making it difficult for the focused study of pristine lunar anorthosites.
76
77 Trace element partitioning in plagioclase is dependent on the anorthite content, which exerts
78 control on the lattice strain parameters (Drake and Weill, 1975; Blundy and Wood, 1991;
79 Bindeman and Davis, 2000; Bédard, 2006; Tepley et al., 2010; Dohmen and Blundy, 2014; Sun
80 et al., 2017). The strong crystal chemical dependence in the plagioclase mineralogy requires any
81 potential lunar crustal material analog involving the study of trace elements to have the closest
82 match in terms of anorthite content. In addition, this warrants the justification for detailed
83 characterization of trace element geochemistry of the potential lunar material analog for both
84 experimental petrology or spectroscopic studies.
85
86 The rare occurrence of megacrysts of anorthite ($An_{97}Ab_3$) were first reported within the basaltic
87 lava flows of Mt. Hyoutanyama on the island arc volcano of Miyake-jima in the Izu islands of
88 Japan (Kikuchi, 1888). The anorthites have ~0.5% FeO and are often noted to be coated by red-
89 wine colored hematite crystallites (Isshiki, 1958; Smith and Brown, 1988; Arakawa et al., 1992).
90 These megacrysts are exhibited to have homogeneous cores lacking typical compositional
91 zoning, which make them ideal as starting materials in experimental petrology and spectroscopic
92 studies investigating lunar material analogs. Amma-Miyasaka and Nakagawa, (2002) suggested a
93 deep-seated plutonic body exists under the island arc and the erupting magma entrains the

anorthite megacrysts occurring on the Miyake-jima island leading to their xenocrystic origin. It might be worth stating here that although high anorthite megacrysts occurrences are rare in general, there have been reports (Kimata et al., 1995) of other plagioclase which have An# > 90 from all over the Izu-Japan island arc system: Hachijo-jima($An_{93.0}$), Hakone ($An_{94.3}$), Sukumogawa ($An_{93.6}$), Sukumoyama ($An_{91.4}$), Otsuki ($An_{93.0}$), Toyaba ($An_{91.3}$), Yoneyama ($An_{92.1}$), Mt. Takahara ($An_{93.8}$), Mt. Nangetsu ($An_{90.3}$), Kayodake ($An_{90.0}$), Fugoppe ($An_{92.7}$), and Kuttara ($An_{91.5}$). These anorthite samples may also be worth considering for material analog in a future study.

Multiple studies on lunar and planetary science have identified Miyake-jima anorthites as a high-quality anorthite feldspar sample owing to its megacrystic occurrence, optical clarity, and homogeneous composition. The RRUFF Project database (https://rruff.info/) also lists this specimen (RRUFF ID: R0400549) along with its major element composition, Raman, X-ray diffraction and infra-red spectra. Initial spectroscopic studies of Miyake-jima anorthite megacrysts have demonstrated the utility of Miyake anorthite as a lunar material analog (Brydges et al., 2015) owing to their highly anorthitic (An_{87-96}) composition (Amma-Miyasaka and Nakagawa, 2002). Additionally, thermal infrared laboratory measurements of these anorthites were used to place constraints on the composition of the Moon's primary anorthositic crust as observed by the Diviner Lunar Radiometer aboard the Lunar Reconnaissance Orbiter based on the position of the Christiansen feature (CF), a known spectral feature that has been shown to be related to An# (e.g., Donaldson Hanna et al., 2014; Donaldson Hanna et al., 2012). Experimental petrology studies have used pulverized Miyake-jima anorthite as starting material that mimics lunar crustal mineralogy in their investigations of Mg-suite magmatism or lunar

magma ocean crystallization (Elardo et al., 2017; Elardo et al., 2020). Branlund and Hofmeister (2012) calculate thermal diffusivities (D) of Miyake-jima anorthites among other natural plagioclase and find that D decreases with increasing An content due to increased disorder. The shocked lunar anorthites have been investigated by using shocked Miyake-jima anorthite analogs to understand the effect of impacts on the anorthite structure (Boslough et al., 1986; Xie et al., 2021). The hydrogen abundances of Miyake-jima anorthite crystals have been measured (Mosenfelder et al., 2015) so they could be used as matrix-matched secondary ion mass spectrometry (SIMS) standard for the measurement of hydrogen in lunar anorthosites (Hui et al. 2017). Miyake-jima anorthites have also been used as standards for oxygen isotope analyses of ordinary chondrites and Itokawa asteroid (Yurimoto et al., 2011). Diffusion coefficients of Mg, Ca and Sr have been investigated by SIMS profiling on Miyake-jima anorthite to understand the evolution of their isotopic systematics in the early solar system history (LaTourrette and Wasserburg, 1998).

Although Miyake-jima anorthites have been identified by the lunar science community as an material analog for the FAN crust, currently no study exists that focuses on the detailed geochemistry of the natural material. Here we present the major, minor, and trace element concentrations of crystal fragments derived from $An_{>90}$ megacrystic anorthite along with their intra- and inter-crystalline variability. We compare our results with the existing geochemical data for different lunar crustal suites and discuss the relevant applications of the Miyake-jima anorthites as lunar crustal material analogs.

2. Methods

We performed electron microprobe, secondary-ion mass spectrometry, and high precision laser-ICP-MS techniques analyses on seven colorless crystal fragments (Supplementary Fig. S1) of Miyake-jima anorthite acquired from the University of Arizona Alfie Norville Gem and Mineral Museum, Tucson, AZ, USA. The anorthite crystals (MG-1 — 7) often occur with some mafic minerals, which were carefully removed by dry (water-free) polishing under ethanol using sandpaper of grit size 200 - 800 and finally with diamond powder of 3- and 1-micron size. Walker et al., (1995) show that turbidity in alkali feldspars is directly correlated to micro-textural features such as microporosity, alteration, fluid inclusion pits, and exsolution. Therefore, clear crystals, which showed exceptional optical clarity and were free of optically visible inclusions, were chosen in this study. These crystals were pressed into a mount of metallic indium to ensure that they are available for future studies involving measurement of volatile species like hydrogen. Additionally, some Miyake-jima megacrysts (Fig. 1) were crushed to particle sizes 75 - 125 μm and 125 - 250 μm and later purified by magnetically separating the anorthite megacrysts from their basaltic coating. These samples are used to conduct the near infrared (NIR) and thermal infrared (TIR) spectral analyses of the Miyake-jima anorthites samples.

2.1. Major and Minor Element Analyses

Major and minor elements in Miyake-jima anorthite were analyzed with a Cameca SX-100 Cameca electron microprobe analyses (EPMA) at the Michael J. Drake Electron Microprobe Laboratory, Lunar and Planetary Laboratory at the University of Arizona. An accelerating potential of 15 kV was used for all the sample analyses. The beam current was 10 nA for Na and K and 20 nA for Si, Ti, Al, Mg, Ca, Fe, Mn, Cr, and P using a 5 μm beam size. Counting times were 10 seconds on peak and 10 seconds on background for Na and K. Counting time was 20

seconds on peak and 20 seconds on background for the remaining elements, in order to improve the counting statistics. The combination of natural crystals and synthetic glasses used as standards were Hakone Anorthite (Al, Ca), Chromite - USNM 117075 (Cr), Rockport Fayalite (Fe), Orthoclase OR-1 (K Si), San Carlos Olivine (Mg), Rhodonite 104791 (Mn), Crete Albite (Na), Synthetic fluorapatite (P), and Natural Rutile (Ti). PAP correction procedures were used to convert specimen/standard intensity ratios into concentrations (Pouchou and Pichoir, 1991). Compositions of electron microprobe standards are listed out in Supplementary Table S1 and individual microprobe measurements are reported in Supplementary Table S3.

2.2. Trace elements

In this section we conduct core to rim analyses of the Miyake-jima anorthite crystals for a suite of trace element data collected using both laser ablation inductively coupled plasma mass spectroscopy (LA-ICP-MS) and secondary ion mass spectrometry (SIMS) techniques.

2.2.1. Laser Ablation - Inductively Coupled Plasma - Mass Spectrometry

Trace element analysis on the anorthite crystals was performed with LA-ICP-MS. Analyses were performed at the METAL Core Facility, Arizona State University using an ESI NWR193^{UC} Excimer ArF Laser Ablation system (Günther et al., 1997) attached to Thermo iCAP-Q ICP-MS. ActiveView software for the laser was coupled by way of bidirectional ethernet communication with the mass spectrometer software, Qtegra, by way of the relevant plugin. This ensured that the sequence timing, laser log files, and sample identification were managed automatically to facilitate subsequent data reduction in Iolite IV (Woodhead et al. 2007; Paton et al. 2011; Pettke et al. 2012). The mass spectrometer was calibrated in solution mode to establish detector cross

calibration factors and define the mass calibration. Forward power was set to 1500 W with gas flows and lens tuning parameters set to optimize signal stability and minimize polyatomic species ($^{232}Th^{16}O$ acting as the main proxy). To reduce the tuning complexity, we also followed the normalized argon index described by Fietzke and Frische, (2016) to efficiently identify a robust tuning condition balanced against sensitivity to yield adequate counting statistics on the most trace analytes during analytical sessions. The fluence of the laser was kept at 60% (~2 J/cm^2). The gas flow of the laser carrier and nebulizer were set at 0.6 L He/min and 0.77 L Ar/min, respectively. Wash-in and wash-out times were intentionally asymmetric to improve workflow automation when selecting signal versus gas blank in the partially automated data reduction run in Iolite IV.

Trace elements and their isotopes analyzed in four LA-ICP-MS sessions are described in Table 1, where the later sessions were used to target elements of low abundance in the anorthite crystals. Most trace elements were analyzed in the first session on the seven selected grains from edge to edge with a spot size of 50 μm, 30 Hz rep rate and 4 μm/s scan speed for ~75 μm long lines. These lines were set up to closely follow the profiles explored in the electron microprobe. Pre-ablation scans were performed with a spot size of 55 μm, 15 Hz rep rate and 30 μm/s scan speed to clean the topmost surface layer. The large spot size and lines were used to target the sample to optimize the accuracy of the data and also address both the inter- and intra-crystalline compositional heterogeneity among different Miyake-jima anorthite crystals. Low abundance elements like HREEs and Th were analyzed in separate sessions: Session II-IV. Therefore, the indium mount with anorthite crystals was re-polished until the ablation pits from previous sessions were no longer visible. New line patterns were laid out such that the regions analyzed

directly underlay the previous ablation pits. HREEs (Gd - Lu) and Th were analyzed in the Sessions II - IV listed in Table 1. Experimental conditions for the low abundance analytes were chosen with a larger spot size of 120 μm with 35 Hz rep rate and 4 μm/s scan speed for lines ranging from 630 - 100 μm in length. Pre-ablation scans in Session II - IV were performed with a spot size of 135 μm, 35 Hz rep rate and 40 μm/s scan speed.

The isotopic acquisitions were manually screened in the Iolite IV software for spikes in Rb: a proxy element, which indicates presence of melt inclusions to ensure reliable (accurate and precise) analysis. The data was carefully surveyed using the Iolite software to note for obvious spikes in Rb compared to the general concentration in the Miyake-jima crystals. Signal bearing such fluctuations or spikes were either partially or completely removed (depending on the spatial extent of the spikes) to ensure that melt inclusions were not sampled as opposed to the pristine anorthite lattice. The NIST SRM 600 series glasses were used as the bracketing standards and tuning was optimized with glass having comparable (by order of magnitude) analyte concentrations for most elements. The analytical sensitivities were evaluated by comparing integrated counts in low-concentration samples and standards with blanks; where prudent, some analytes had increased dwell time to improve counting statistics in the Qtegra software running the quadrupole ICP-MS. The internal standardization in Session I was achieved by analysis of calcium in the anorthite crystals from electron microprobe (Table 2). The choice of calcium as the internal standard hinged on (i) its high abundance (13.83 - 13.97%) and homogeneity within the Miyake-jima anorthite crystal cores and furthermore, (ii) calcium provides the opportunity for comparing our results to the external reference materials BCR-2G and BHVO-2G (Gao et al. 2002), which were also analyzed using the same internal standard. In Sessions II-IV, lanthanum

(La) served as the internal standard because of its (i) high abundance (0.0216 - 0.0290 ppm) relative to trace elements measured in Session II-IV, (ii) its homogeneity as discussed in the results section of this study, (iii) lack of polyatomic interferences (May and Wiedmeyer 1998), and (iv) proximity to the analytes, HREEs and Th, in terms of the masses analyzed. The consistently flat profiles obtained for La with low standard deviations from session I provided the rationale to use it for measuring sub-ppb concentration of HREEs and Th. Furthermore, La when used as the internal standard removed the need for the electromagnet to sweep across a large range of masses as it would have been the case if Ca was employed as the internal standard instead, Ultimately this allowed us to obtain increased dwell times and therefore enhanced counts on the low abundance target analytes.

Two relatively abundant copper isotopes ^{63}Cu and ^{65}Cu were analyzed to check for interference between ^{63}Cu and $^{23}Na^{40}Ar$. Oxide (Th/ThO) production rates were monitored and observed to be < 1% throughout the duration of the analytical session, which is also an indicator of robust plasma conditions balancing for signal-to-noise ratio for the analytes while keeping polyatomic species relatively low. The robust plasma conditions facilitate analysis of non-matrix matched calibration standards and bracketing standards for LA-ICP-MS signals (e.g., Heinrich et al., 2003). Though imperfect, the NIST SRM 600 series glass standards provided the best available material for calibration, having similar ablation thresholds, and concentration ranges for many analytes. Moreover, our selected standards allowed suitably accurate results for external standards as described below.

Data reduction was performed using Iolite software using the “Trace Elements Next” Data

Reduction Scheme (DRS). To maintain objectivity, where possible, automatic selections were employed for baseline and sample region selections. All time-series traces were carefully inspected for possible anomalies such as melt inclusions (described above). The accuracy of measurements during Session I were tested by measurement of external standard BCR-2G and BHVO-2G between every 3 - 4 analyses. The measured concentrations from the external standards have been compared with the values reported by Gao et al., (2002) with LA-ICP-MS (Supplementary Fig. S2). Based on a total of 24 BCR-2G and BHVO-2G measurements on external standards recorded during Session I, the relative errors with respect to Gao et al. (2002) for the trace elements are approximately within the 20% for BCR-2G and 25% for BHVO-2G (Supplementary Fig. S2). 1-σ standard deviation error bars represent the reproducibility of the analyses during Session I, which are less than 9%. Individual analyses of BCR-2G and BHVO-2G external reference material is reported in Supplementary Table S2. The two copper isotopes, ^{63}Cu and ^{65}Cu, display good agreement among the natural anorthite samples with the slope approximating one and intercept close to origin (Supplementary Fig. S3). This established that there is negligible interference between ^{63}Cu and $^{23}Na^{40}Ar$.

2.2.2. Secondary Ion Mass Spectrometry

Depth profiles of minor and trace elements Na, K, Ti, and Li were measured using the Ametek Cameca IMS6f SIMS at the NSF National Facility at Arizona State University. A primary beam of O_2^- was accelerated to 12.5 keV, focused to a spot, and rastered over a 20 × 20 μm^2 area to sputter a flat crater. A 400 μm field aperture allowed ions from a 15 μm diameter circular area in the center of the sputtered crater into the mass spectrometer, eliminating ions derived from the crater walls. Positive secondary ions were accelerated to 9000 eV. The following ion intensities

were collected: ^{7}Li, ^{23}Na, ^{39}K, ^{47}Ti, and ^{30}Si. All secondary ion signals were normalized to the count rate for $^{30}Si^{+}$, a matrix ion. Secondary ions were examined with 0 ± 20 eV energy and no energy filtering was applied. The primary beam current of ~5 nA and the pressure in the analytical chamber varied from 1.13×10^{-9} to 0.75×10^{-9} torr over the analytical session.

The sample was pre-sputtered for 180 s at the beginning of each analysis to lower the probability of analyzing K present as surface contamination. Interference between ^{39}K and $^{23}Na^{16}O$ was resolved by closing the entrance and exit slits of the mass spectrometer to cleanly separate these two species ($M/\Delta M < 2000$). Any interferences on Ti were also resolved at this mass resolving power. Note that the abundant ^{48}Ti isotope was not used because of the unresolvable interference from ^{48}Ca. A single cycle took ~ 11 s, including waiting time to settle the magnetic field at each mass. Peaks for each of the different isotopes were detected by either the electron multiplier (EM) or Faraday Cup (FC) secondary ion detectors in the following order: ^{7}Li (1 s, EM), ^{23}Na (1 s, FC), ^{39}K (2 s, FC), ^{47}Ti (1 s, EM), and ^{30}Si (1 s, EM). NIST series glasses -610, -612, -614, -620. and GSE were used to calibrate the Li, Na, K, and Ti concentrations in anorthite. Over the course of the analyses, charge was compensated by moving the magnetic field to detect ^{30}Si and the sample voltage was ramped from 8901 to 8801 V every 5th cycle. The sample voltage was placed at the centroid of the voltage vs secondary ion intensity curve. The charge compensation routine was similar to the process described in Shamloo et al. (2021). The largest 2-sigma standard errors for the ion ratios recorded are $^{7}Li/^{30}Si$ (2.8%), $^{23}Na/^{30}Si$ (0.36%), $^{39}K/^{30}Si$ (1.42%), and $^{47}Ti/^{30}Si$ (1.88%).

2.3. Near and thermal infrared spectroscopy

We acquired near infrared (NIR) reflectance and thermal infrared (TIR) emissivity measurements within the Planetary Spectroscopy Facility at the University of Oxford. Miyake-jima megacrysts coated in basalt were initially crushed and sieved into size fractions of 75-125 μm and 125-250 μm and washed with distilled water for magnetic separation. Anorthite megacryst materials were separated from their basaltic coating and mafic inclusions by putting each particle size fraction through a Frantz magnetic separator. Each particle size fraction was run through the Frantz at least three times until only the anorthite particles remained in the non-magnetic fraction as determined in a microscope. Once magnetically separated, the sample was further crushed and sieved into < 25 μm and 125-250 μm particle size fractions. The 125-250 μm particle size fraction was used for near infrared reflectance measurements as this particle size fraction is ideal for highlighting diagnostic spectral features in the NIR, while the < 25 μm particle size fraction was used for thermal infrared emissivity measurements as this particle size fraction is the spectrally dominant particle size at TIR wavelengths.

NIR reflectance measurements were made using a Brüker IFS 66v Fourier Transform Infrared (FTIR) spectrometer with a Specac^{TM} Diffuse Reflectance FTIR Accessory, a CaF_2 beamsplitter and a deuterated triglycine sulfate (DTGS) detector. The measurements were taken at a resolution of 2 cm^{-1} from ~0.8 to 5 using a 12 mm aperture, 2.2 kHz scanner velocity, and 125 scans. TIR emissivity measurements were made under ambient ('Earth-like') and simulated lunar environment (SLE) conditions using the Planetary Analogue Surface Chamber for Asteroid and Lunar Environment (PASCALE) chamber (Donaldson Hanna et al., 2021). PASCALE is mounted to the emission port of a Bruker VERTEX 70v Fourier Transform Infrared (FTIR) spectrometer using a cesium iodide (CsI) window. Thermal infrared spectra were measured at a

resolution of 4 cm^{-1} from ~2400 to 200 cm^{-1} (~5 to 50 mm) using a wide-range TIR beamsplitter and a deuterated, L-alanine doped triglycine sulfate (DLaTGS) detector. Three measurements of 250 scans were made of each sample, which produces a spectrum with sufficient signal-to-noise such that we can uniquely identify features of 2% contrast from the noise. The final TIR spectrum for each sample is an average that has been calibrated using published methods [e.g., Ruff et al., 1997] and spectral measurements of a calibration target painted with Nextel high emissivity black paint at 340 and 360 K [e.g., Thomas et al., 2012]. The near-surface conditions of the lunar regolith are simulated by creating thermal gradients similar to those experienced on the Moon. Thermal gradients are created in the uppermost position of the lunar soils by evacuating the chamber to vacuum pressures ($< 10^{-4}$ mbar), by cooling the interior of the chamber to < 125 K using liquid nitrogen (LN_2), and heating the samples from below and above to brightness temperatures similar to those on the Moon [e.g., Donaldson Hanna et al. 2017; Williams et al., 2017].

3. Results

We present the chemical data of the Miyake-jima crystals obtained from the analytical instruments employed in this study – electron microprobe, LA-ICP-MS and SIMS. This section focuses on the crystal core compositions, intra- and inter-crystalline heterogeneity and highlights the reproducibility of elemental data across the different analytical approaches applied to target the Miyake-jima sample suite.

3.1. Variability of Mineral Chemistry

We employ all three analytical techniques – electron microprobe, LA-ICP-MS, and SIMS to target the variability of major, minor and trace chemical composition within individual anorthite crystal lattice as well as across the sample set.

3.1.1. Major and minor elements

Table 2 lists the average electron microprobe analyses of cores and rims of each Miyake-jima grain chosen in this study. Individual analyses across the profiles (shown in Fig. 2) are listed in the Supplementary Table S3. MG-4 and MG-7 show distinct bytownite (An_{86-87}) margins of ~25 micrometers surrounding the homogeneous core. Calculations of anorthite composition do not include the K-feldspar end-member due to K being present only in trace quantities. Fig. 2 shows that SiO_2 and Al_2O_3 wt% vary stoichiometrically near the bytownitic rims – SiO_2 increases from ~ 44% to ~ 46% and Al_2O_3 decreases from ~ 36% to ~ 33%. The high albite margins of MG-4 and MG-7 exhibit more drastic fluctuations in MgO (increase from ~ 0.08% to ~ 0.14%) and FeO (increases from ~ 0.43% to ~ 0.85%) also seen in Fig. 2. Measurements of other elements (Ti, Mn, Cr, K, and P) were consistently below their respective EPMA detection limits. The approximate detection limits of the electron microprobe analyses are: Ti 220 ppm, Mn 500 ppm, Cr 230 ppm, K 350 ppm, and P 300 ppm.

3.1.2. Trace elements

SIMS analyses show that the bytownitic rims are contrasting in both trace elements as well as major element compositions. As per Fig. 3, with respect to the core, the rims are enriched in Li (by 1.5 – 3.5 times), K (by 1.2 – 2.4 times), Na (by ~1.7 times), and Ti by (by 1.1 - 1.2 times). It must be noted that the true bytownite rim may have been only partially captured in MG-4 and

MG-7 during SIMS analysis due to there being no optical differences between the domains. Other crystals chosen in this study lacked any distinctly heterogeneous margin and capture the heterogeneity in the cores of Miyake-jima anorthites. Li, K, Na, and Ti concentrations with 1-σ errors for the cores of the seven Miyake-jima grains are 0.31 ± 0.14 ppm, 44.01 ± 3.77 ppm, 3510 ± 461 ppm, and 37.29 ± 2.93 ppm respectively for the calibration constructed with the both GSE and NIST-series glasses. Table 3. shows summarizes the trace element concentrations derived from 14 SIMS analyses performed on the Miyake-jima anorthite grains. Individual SIMS analyses are in Supplementary Table S4.

LA-ICP-MS analyses were unable to capture the rims of the Miyake-jima crystals due to the larger spot size (135 μm) of analyses compared to the narrow and restricted rims (<25 μm) of the anorthites. Therefore, the trace element data derived from the ICP-MS is directed towards exploring the inter-crystalline heterogeneity and/or homogeneity of individual crystal cores. Trace element data for grain domains collected over all ICP-MS sessions are compiled in Table 4. Individual trace element analyses from all LA-ICP-MS sessions are reported in Supplementary Table S2. In Table 5, we report the summative average major, minor, and trace element composition of all Miyake-jima anorthites crystals analyzed in this study.

For illustrative purposes, Fig. 4 shows the profile of two grains MG-4 and MG-7, which had distinct rims observed in terms of major elements. The profiles for the other grains are in the Supplementary Fig. S4. MG-4 shows a prominent elevation of all LREEs by about one order of magnitude towards the margin of the Miyake-jima crystal. The profile for MG-7 was unable to capture the “true” rim of the grain possibly because the large laser spot likely overlapped onto

the more homogeneous crystal interior. Table 6 shows the 1-sigma percentage standard deviations for each LREEs measured for cores of all Miyake-jima samples in the LA-ICP-MS. The largest standard deviations recorded is 30.91 with most percent standard deviations being within 10-20%, shows that the LREEs are homogeneously distributed in the cores of the Miyake-jima anorthites. The inter-crystalline homogeneity is also evident from Fig. 4 and Supplementary Fig. S4.

Thorium concentrations were below detection limits in all LA-ICP-MS sessions, except a few analyses in Session IV. The increased dwell time from 0.01 s to 0.10 s on ^{232}Th in Session IV helped improve the sensitivity for thorium measurements (see Supplementary Fig. S5). It may be noted that detection limits improve (i.e., decrease) from Session I to Session IV as a result of increased effective dwell time on thorium and thus improved sensitivity. Thorium has been measured above the limit of detection (LODs; calculated according to Pettke et al. 2012) for only MG-2 and 7 in Session IV. However, the thorium concentrations for MG-2 have lower confidence because their 2-σ uncertainties overlap the LODs. The best thorium analyses above detection limits with 2-σ errors are from MG-7: 0.122 ± 0.035, 0.026 ± 0.015, and 0.015 ± 0.010 ppb.

3.2. NIR and TIR Spectral Measurements

The NIR reflectance measurement of the 125-250 μm particle size fraction confirms the crystalline nature of the Miyake-jima anorthite megacrysts as it has a distinct absorption band near 1.25 μm due to minor amounts of Fe^{2+} in the crystal structure (see Fig. 5). The lack of NIR diagnostic absorption bands near 1.0 and 2.0 μm demonstrates that the basaltic coating and mafic

415 inclusions have been effectively removed and the sample is composed entirely of the anorthite
416 core crystal material. At these wavelengths, the spectra of other terrestrial anorthites are often
417 affected by the Earth's weathering process that act to remove the diagnostic absorption feature
418 near 1.25 μm and introduce additional features from accessory minerals complicating the spectral
419 signature (e.g., Adams and Goullaud, 1978). The TIR emissivity measurements made under
420 ambient and simulated lunar environment (SLE) conditions of the < 25 μm particle size fraction
421 have spectral features consistent with highly calcic plagioclase. Specifically, the Christiansen
422 feature (CF) positions identified in the ambient and SLE spectra of Miyake-jima anorthite
423 (1233.9 and 1275.6 cm^{-1}, respectively) are similar to terrestrial anorthites previously measured in
424 the lab (e.g., Nash and Salisbury, 1991; Milam et al., 2004; Donaldson Hanna et al., 2012;
425 Donaldson Hanna et al., 2014). However, we do observe differences between the Miyake-jima
426 anorthite spectra and previously published terrestrial anorthite spectra. Specifically, we find that
427 the position of spectral features including the transparency feature (TF) and vibration bands are
428 at lower frequencies (longer wavelengths) than previously measured terrestrial anorthite spectra
429 that are less calcic than the Miyake-jima anorthites. Additionally, we observe (1) that the shape
430 of these spectral features are more distinct (less rounded) and (2) weaker vibration band features
431 (spectral contrasts ≤ 3%) that were not previously identified in lab spectra of terrestrial
432 anorthites, both which could result from the crystalline nature of the Miyake-jima anorthites
433 and/or the improved spectral resolution of our laboratory measurements. Finally, similar to the
434 NIR measurements, no spectral features owing to the basaltic coating and mafic inclusions are
435 observed in the TIR spectra.

436 ## 3.3. Comparison of Analytical Techniques

437 The precision and accuracy of Ti and Na were independently examined by comparing the results

obtained from the electron microprobe, LA-ICP-MS, and SIMS analytical techniques. (Supplementary Fig. S6) shows the Ti and Na ppm concentrations measured for the cores of the seven selected grains. 1-sigma errors on the microprobe measurements of the Na in the cores are considerably larger than the considerably more precise SIMS estimations for Na. The electron microprobe analyses on Supplementary Fig. S6a were chosen carefully to spatially overlap with the area rastered by the SIMS analysis. Although in close proximity, it may be noted that the points shown in Supplementary Fig. S6a do not have a volumetric overlap since the sample excitation volume for electron microprobe is much smaller than the volume sputtered by the ion microprobe. The comparison between the different analytical techniques is a collective reflection of the volumetric heterogeneity within individual anorthite crystal cores, and the effect of different instrumental and analytical parameters. The intracrystalline and intercrystalline heterogeneity for Na is high because their concentrations vary by ~1500 ppm (based on SIMS and EPMA) and plot on either side of the 1:1 line (Supplementary Fig. S6b). The Ti concentrations derived from individual SIMS analyses are systematically underestimated in comparison to the LA-ICP-MS measurements, by a factor of 0.78 – 0.94. For Ti, 1-sigma standard deviation of the population from multiple LA-ICP-MS measurements are comparable with the seven individual SIMS analyses of the seven Miyake-jima grain cores. A reduction in the systematic errors is noted in (Supplementary Fig. S6b) for the Ti concentrations derived from SIMS when calibrated against only GSE glasses in contrast to a combination of GSE and NIST-series glasses. We note an improvement of the correlation factor (slope in Supplementary Fig. S6b) from 0.88 to 0.99 when using the calibration with GSE glass only. The underestimation of Ti from the calibration including NIST-series glasses is due to the high SiO_2 content (~70%) in the NIST matrix compared to the anorthites. The matrix of the GSE glasses ($SiO_2 \approx 43.7\%$) is a

461 better match for the anorthites ($SiO_2 \approx 43.7\%$) compared to the NIST matrix. The dependence of
462 Ti ion yield on the SiO_2 matrix has been documented by Behr et al. (2011). However,
463 measurements from both analytical techniques indicate that inter- and intra-crystalline
464 homogeneity is high for titanium. Comparisons for Li and K are not shown here as Li was not
465 measured by any other technique while K was below the detection limit (~350 ppm) for the
466 electron microprobe.

467

468 ## 4. Discussion

469 Average core compositions across all crystals range from An# = 95.17 - 96.03 (Fig. 6), which
470 confirms the compositional homogeneity of the anorthite crystal cores as reported by Amma-
471 Miyasaka and Nakagawa, (2002). Some unfragmented crystals show bytownite rims of < 25 μm.
472 These crystal margins are notably enriched in Fe, Mg, Li, Ti, K and REEs. Within the sample
473 suite, only MG-4 (see Fig. 4) shows a prominent elevated LREE signature in the crystal rim.
474 Whether this feature is limited only to only one sample or is permeating throughout the sample
475 suite is not clear. However, these rims are not optically distinct from the homogeneous high-An
476 cores. Although these lower-Ca rims have been observed during mirco-analysis, their volume
477 (3.8 - 8.3 vol%, assuming spherical geometry of the crystals) is negligible for analyses and
478 experiments requiring crushed sample. Prior to spectral characterization the basaltic coatings
479 were removed by magnetic separation which was also confirmed by absence of any NIR
480 diagnostic absorption bands near 1.0 and 2.0 μm. However, since the bytownitic rims are not
481 optically or magnetically different from the anorthite cores, they could not be identified and
482 effectively separated. But since the bytownite rims have An# ranging from 85 – 88 and have a

483 minor presence, and are mixed in with the more anorthitic cores, VNIR and TIR spectral features
484 owing to minor amounts of bytownite are not observed. This is not surprising for two reasons:
485 (1) At TIR wavelengths, it has been demonstrated that a material must comprise at least 5-10
486 volume % of a spectrally distinct material to contribute to the overall spectral signature (e.g.,
487 Ramsey and Christensen, 1998). (2) Cheek and Pieters (2014) showed that an intermediate
488 plagioclase sample had the same VNIR band position at 1.25 μm as that of highly-calcic
489 plagioclase.

490

491 The REE patterns (Fig. 7) of all the Miyake-jima anorthite grain cores chosen in this study are
492 subchondritic, have a negative slope i.e., are dominated in the LREEs with progressive HREE
493 depletion. The homogeneous LREE distribution across the cores of Miyake-jima crystals are
494 evident from (i) the small 1-sigma percent standard deviations reported in Table 5, (ii) small
495 error bars shown in Fig. 7, and (iii) considerably flat individual LREE measurements across the
496 crystal core (Fig. 4; Supplementary Fig. 4). All the plagioclase grains have variable but positive
497 Eu anomaly (Eu/Eu* = 11.7 - 21.1, where Eu* is the square root mean of the product of
498 chondrite-normalized Sm and Gd). The best concentrations of low concentration thorium ranges
499 from 0.122 - 0.015 ppb indicating the very low concentration of trace elements. Murakami
500 (1991) identified crystallographically oriented native copper inclusions within the Miyake-jima
501 lattice, however we did not observe such inclusions in both optical and electron images. Neither
502 were any notable spikes or fluctuations in the signal of copper observed during the time resolved
503 analysis which would correspond to the laser ablating copper inclusions.

504 The NIR reflectance absorption band near 1.25 μm (Fig. 5) is able to detect the minor Fe^{+2}

present in the crystal structure can be partly attributed to the 0.45 ± 0.02 wt% FeO determined by the electron microprobe measurements. TIR emissivity measurements and diagnostic spectral features are consistent with high-Ca plagioclase (Fig. 5). Across TIR wavelengths, it has been demonstrated that the position of diagnostic spectral features (i.e., Christiansen feature, vibration bands, and transparency feature) shift as a function of An# (Nash and Salisbury, 1991; Milam et al., 2004; Donaldson Hanna et al., 2012). Therefore, when comparing laboratory measurements to remote sensing observations, it is important for lunar material analogs to have compositions similar to the Moon like the Miyake-jima anorthites. Thus, Miyake-jima anorthite megacrysts are unique in that they have the necessary spectral features of crystalline, highly calcic anorthite across the NIR and TIR spectral ranges for use as a spectral material analog for the Moon.

5. Implications

Natural phenocrystic plagioclase crystals typically show some form of growth zoning (e.g., oscillatory zoning) due to the lack of chemical equilibration and sluggish diffusion kinematics. In that light, the homogeneous cores of the Miyake-jima anorthite crystals are unusual since they do not show any evidence of magmatic zoning except for the narrow bytownite rims. These anorthites have a greater value and potential to be used as an analog or standard material because of them not only having achieved intragranular chemical homogeneity but also intergranular chemical homogeneity due to their overlapping compositions (Fig. 6) within 1-sigma uncertainties. The average Miyake-jima anorthite core composition with 1-σ uncertainties for the seven individual grains is $An_{95.51 \pm 0.31}$.

The highly homogeneous character of the Miyake-jima anorthite crystals and their matrix closely resembling lunar anorthites provide a strong rationale for their potential applications in experimental petrology, SIMS analyses, remote sensing and geophysics. The applications

528 discussed for the lunar material analog, Miyake-jima anorthite, can be used to improve the
529 characterization of lunar crustal material and thereby improving our current understanding of the
530 formation and evolution of lunar crust.
531
532 **5.1. Application in experimental petrology**
533 The unaltered and highly homogeneous nature of the major elements (Ca, Si, Al, and Na) of the
534 Miyake-jima crystal cores render them useful as starting materials for experimental studies.
535 Their close match with lunar anorthite compositions in terms of anorthite contents of An_{96-98},
536 (Papike et al., 1997; McGee, 1993) also make them suitable for experimental studies focused on
537 lunar petrology. Although we observe the presence of bytownite rims in the margins of two of
538 the seven selected samples, their volume contribution would have a negligible effect on the bulk
539 anorthite composition of the starting material. Under lunar lower crustal conditions of ~0.3 GPa,
540 the An_{95} solidus temperatures are greater than 1500°C (Lindsley, 1969). The large pristine crack-
541 free megacrysts may be used to fabricate capsules in lunar crustal assimilation experiments
542 owing to the refractory nature of highly calcic plagioclase. Fig. 8 illustrates that Miyake-jima
543 core anorthite contents are tailing the lower end of lunar FAN anorthite compositions. The cores
544 are slightly enhanced in FeO by ~3.9 times and indistinguishable in MgO content as compared to
545 plagioclase from ferroan anorthosites.
546
547 The concentrations of REEs in the Miyake-jima crystals are 3 - 6 times lower than that in FAN
548 (ferroan anorthosite), HMS (high-magnesium suite), and HAS (high alkali suite) as illustrated in
549 Fig. 9. Most trace elements (see Fig. 10) are within or below the lunar plagioclase concentration
550 range, except for Li and Sr, which are approaching the upper boundary of the lunar FAN sample

suite. Also the trace element concentrations across the grains have a low dispersion (the largest percent standard deviation recorded among the LREEs was noted to be ~31%, see Table 5) and show homogeneous distribution of major, minor, and trace elements in the crystal lattice. The low trace element concentrations compared to lunar plagioclase, the relative homogeneity in trace elements across grains, and also their megacrystic occurrence render the Miyake-jima anorthite crystals as an ideal "blank" that can be doped with trace elements as needed for chemical and spectroscopic studies applicable for high anorthite lunar plagioclase compositions. Day et al., (2019) reports 3.64 ppm of copper in the bulk lunar anorthosite measurement from 66095 or 'Rusty Rock' which is comparable with the Miyake-jima copper concentrations of 1.40 – 1.43 ppm (Table 6). Furthermore, considering that Murakami (1991) identified copper inclusions in the Miyake-jima samples, it is probably best not to use Miyake-jima anorthites as a blank slate for copper. A specific REE or any other trace element (except copper) that have low abundance may be artificially doped within these plagioclase crystals to elevate their abundances closer to lunar suites (FAN/HMS/HAS), making them more representative. In experiments involving lunar petrology, the trace element concentrations of Miyake-jima anorthites can be adjusted as desired since this study reports what the "blank" levels are to begin with.

5.2. Application as standard reference material for secondary ion mass spectrometry (SIMS)

The most accurate SIMS analyses use matrix-matched (mineralogically and chemically consistent) standards and analytes because secondary ion yields often vary with major element chemistry (e.g., Shimizu and Hart, 1982; Mosenfelder et al., 2015). The viability of using Miyake-jima anorthites ("GRR1968" as described in Mosenfelder et al., 2015) for measuring

574 hydrogen in lunar plagioclase has already been demonstrated by Hui et al., (2017). Hydrogen
575 abundances determined by FTIR range from 58 ± 6 to 73 ± 8 ppmw for Miyake-jima anorthites
576 (Mosenfelder et al., 2015). Although the core-rim heterogeneity for H has not been investigated
577 for Miyake-jima anorthites yet, we do report in this study that the cores are homogeneous in
578 terms of major and trace elements (see Fig. 2 and Fig. 4). This provides a uniform matrix-
579 matched substrate that can be dehydrated to make blanks and also doped/implanted with desired
580 trace elements to synthesize appropriate sets of lunar crustal reference materials for future SIMS
581 or nanoSIMS investigations.
582
583 Yurimoto et al., (2011) measured the oxygen isotopic composition of Miyake-jima to be
584 $\delta^{17}O_{SMOW}$ = 3.33 ± 0.3‰ (2σ) and $\delta^{18}O_{SMOW}$ = 6.40 ± 0.4‰ (2σ) which shows a high degree of
585 sample homogeneity demonstrating its application as a standard material for SIMS
586 measurements. Our thorough investigation of the major element chemistry highlights the
587 homogeneous matrix is well suited for ion microprobe analyses. LaTourrette and Wasserburg,
588 (1998) have successfully exploited the homogeneous nature of the Miyake-jima crystal to their
589 advantage and measured diffusion coefficients of Mg, Ca and Sr using SIMS to understand the
590 thermal evolution of early formed planetesimals.
591

592 ### 5.3. Application to remote sensing observations of the Moon and other airless
593 bodies

594 Across the near infrared portion of the electromagnetic spectrum, crystalline plagioclase
595 feldspars can be identified by their characteristic 1.25 μm spectral feature owing to minor
596 amounts of Fe^{2+} in the crystal structure. The wavelength position of the 1.25 μm absorption band

does not systematically change with calcium content (Adams and Goullaud, 1979), thus its wavelength position cannot be used to uniquely determine the An# of plagioclase feldspar. On the Moon and other airless bodies, the depth of the 1.25 μm absorption band can be affected by several factors. First, the depth of the band has been shown to systematically increase with an increase in abundance of Fe being incorporated into the crystal structure (e.g., Cheek et al., 2010; Cheek et al., 2011). Second, the 1.25 μm absorption band can be weakened (i.e., reduced in strength) to the point of disappearance by space weathering (e.g., Lucey, 2002) and shock metamorphism (e.g., Spudis et al., 1984). At thermal infrared wavelengths, the wavelength position of diagnostic spectral features including the Christiansen feature, fundamental vibration bands (also known as the reststrahlen bands), and the transparency feature have been shown to shift systematically to higher frequencies (longer wavelengths) as the calcium content in plagioclase feldspar increases (Nash and Salisbury, 1991; Milam et al., 2004; Donaldson Hanna et al., 2012). The spectral features, in particular the vibration bands and transparency feature, identified in the Miyake-jima anorthite TIR emissivity spectra are at higher frequencies (longer wavelengths) than previously studied terrestrial anorthite samples that are less calcic than Miyake-jima anorthites. Additionally, the crystalline nature of the Miyake-jima megacrysts result in TIR spectra that have more distinct spectral features than previous lab studies of terrestrial anorthites. All of this suggests that lab measurements of Miyake-jima anorthite spectra are necessary for interpreting future hyperspectral observations of the Moon, especially regions identified as pure anorthosites (PANs; e.g., Ohtake et al., 2009; Cheek et al., 2013; Donaldson Hanna et al., 2014).

To best interpret remote sensing observations of the Moon's primary anorthositic crust, especially those that include near and thermal infrared observations, the plagioclase terrestrial

620 material analog being used must be: (1) crystalline in nature and (2) have an An# similar to that
621 of plagioclase within the FANs. Currently, the only known terrestrial material analog that fits
622 these parameters are the Miyake-jima anorthite megacrysts (assuming the basaltic coating and
623 mafic inclusions have been removed). Initial laboratory studies have begun with the pure mineral
624 endmember of Miyake anorthite (Donaldson Hanna et al. 2014) and with mixtures of Miyake
625 anorthite and mafic minerals olivine and pyroxene (Arnold et al., 2016; Greenhagen et al., 2020).
626 Future comparisons of NIR and TIR remote sensing observations of the Moon and laboratory
627 measurements of these types of material analog samples will be critical in better understanding
628 the formation and evolution of the anorthositic crust and the distribution of crustal materials
629 across the lunar surface.
630

631 ### 5.4. Application to Geophysical Properties

632 Branlund and Hofmeister, (2012) measure thermal diffusivity (D) of anorthite with Miyake-jima
633 samples between 298 – 1050 K. They also note low D_{298} values compared to other plagioclase,
634 along with variation along different crystallographic axes with D_{298} values ranging from 0.682 –
635 0.755. Understanding the thermal properties of Miyake-jima anorthite can improve our
636 understanding of conductive heat transfer through the lunar anorthosite "crustal lid" and model
637 the thermal state of the Moon's interior from the magma ocean state to the present. Additionally,
638 the Miyake-jima anorthites can also be used to constrain electric resistivities which in turn have
639 their direct application in understanding the nature of the present day selenotherm (or thermal
640 state) since the bulk of the lunar crust is dominated by anorthositic plagioclase.
641 Wang et al., (1973) measured the elastic properties of aggregates of plagioclase which have been
642 coupled with seismic discontinuities to understand the crustal structure and density of

643 microcracks in the lunar interior. The study of elastic properties of Miyake-jima anorthites which
644 is a closer compositional and structural match with the FAN suites can potentially improve the
645 current understanding of the seismic signals from the shallow lunar crust. Finally, the since the
646 densely cratered structure of the Moon's older FAN highlands would most certainly have
647 evidence of shock features, Miyake-jima crystals can be a great material analog for studying
648 (Pernet-Fischer et al., 2017) the impact history of the lunar crust. Shocked Miyake-jima samples
649 have also been used to derive the Hugoniot equation (Boslough et al., 1986) and the effect of
650 shock on the Raman spectra (Xie et al., 2021) which highlight Miyake-jima anorthites as a
651 popular choice in understanding shocked feldspars as analogs of lunar crust.
652

653 ## 6. Acknowledgements

654 We thank Eric Fritz from the University of Arizona Alfie Norville Gem and Mineral Museum in
655 Tucson for the gem quality crystals of Miyake-jima anorthite. The Miyake-jima megacrysts for
656 spectral analyses were obtained from Alfredo Petrov. For support and assistance with analytical
657 techniques, we thank Kenneth Domanik (electron microprobe, University of Arizona) and Lynda
658 Williams (SIMS, Arizona State University supported by NSF EAR 1819550). We acknowledge
659 Jessica Barnes (University of Arizona) for teaching us how to mount samples in indium. We
660 extend our gratitude to Jan Fietzke (GEOMAR Helmholtz Center for Ocean Research, Kiel) and
661 Jason Kirk (University of Arizona) for constructive feedback on expected challenges in LA-
662 ICPMS for low-signal trace element measurement work undertaken in this study. We also thank
663 Thomas Prettyman (Planetary Science Institute) for providing valuable feedback regarding the
664 application of these samples in spectroscopy. We acknowledge the insightful comments from
665 one anonymous reviewer and Neil Bennett and Associate Editor Daniel Hummer. A.R.

acknowledges support from the Galileo Circle scholarships and the Mineralogical Society of America grant for student research in Mineralogy and Petrology. A.M. acknowledges NASA grant # 80NSSC24K0543 and her startup grant from the Office for Research, Innovation, and Impact and Eminent Scholar Funds from the College of Science at the University of Arizona.

7. References

Adams, J.B., and Goullaud, L.H. (1978) Plagioclase feldspars - Visible and near infrared diffuse reflectance spectra as applied to remote sensing. 9th Lunar and Planetary Science Conference, 3, 2901–2909.

Amma-Miyasaka, M., and Nakagawa, M. (2002) Origin of anorthite and olivine megacrysts in island-arc tholeiites: petrological study of 1940 and 1962 ejecta from Miyake-jima volcano, Izu-Mariana arc. Journal of Volcanology and Geothermal Research, 117, 263–283.

Arakawa, Y., Murakami, H., Kimata, M., and Shimoda, S. (1992) Strontium isotope compositions of anorthite and olivine phenocrysts in basaltic lavas and scorias of

Miyakejima volcano, Japan. Journal of Mineralogy, Petrology and Economic Geology, 87, 226–239.

Arculus, R.J., and Wills, K.J.A. (1980) The Petrology of Plutonic Blocks and Inclusions from the Lesser Antilles Island Arc. Journal of Petrology, 21, 743–799.

Arnold, J.A., Glotch, T.D., Lucey, P.G., Song, E., Thomas, I.R., Bowles, N.E., and Greenhagen, B.T. (2016) Constraints on olivine-rich rock types on the Moon as observed by Diviner and M3 : Implications for the formation of the lunar crust. Journal of Geophysical Research: Planets, 121, 1342–1361.

Bédard, J.H. (2006) Trace element partitioning in plagioclase feldspar. Geochimica et Cosmochimica Acta, 70, 3717–3742.

Behr, W.M., Thomas, J.B., and Hervig, R.L. (2011) Calibrating Ti concentrations in quartz for SIMS determinations using NIST silicate glasses and application to the TitaniQ geothermobarometer. American Mineralogist, 96, 1100–1106.

Bindeman, I.N. (2007) Erratum to I. N. Bindeman, A. M. Davis, and M. J. Drake (1998), "Ion microprobe study of plagioclase-basalt partition experiments at natural concentration levels of trace elements," Geochimica Cosmochimica Acta 62, 1175–1193, Geochimica et Cosmochimica Acta, 71, 2414.

Bindeman, I.N., and Davis, A.M. (2000) Trace element partitioning between plagioclase and melt: investigation of dopant influence on partition behavior. Geochimica et Cosmochimica Acta, 64, 2863–2878.

Bindeman, I.N., Davis, A.M., and Drake, M.J. (1998) Ion Microprobe Study of Plagioclase-Basalt Partition Experiments at Natural Concentration Levels of Trace Elements. Geochimica et Cosmochimica Acta, 62, 1175–1193.

Blundy, J.D., and Wood, B.J. (1991) Crystal-chemical controls on the partitioning of Sr and Ba between plagioclase feldspar, silicate melts, and hydrothermal solutions. Geochimica et Cosmochimica Acta, 55, 193–209.

Boslough, M.B., Rigden, S.M., and Ahrens, T.J. (1986) Hugoniot equation of state of anorthite glass and lunar anorthosite, Geophysical Journal International. 84, 455–473.

Bowen, N.L. (1917) The Problem of the Anorthosites. The Journal of Geology, 25, 3, 209–243.

Branlund, J.M., and Hofmeister, A.M. (2012) Heat transfer in plagioclase feldspars. American Mineralogist, 97, 1145–1154.

Brophy, J.G. (1986) The Cold Bay Volcanic Center, Aleutian Volcanic Arc. Contributions to Mineralogy and Petrology, 93, 368–380.

Brydges, T.F.V., Marriner, C.M., Donaldson Hanna, K.L., Bowles, N.E., and MacDonald R. (2015) Characterisation of Miyake-Jima Anorthite as a Lunar Analogue. 46th Lunar and Planetary Science Conference, 1251.

Cahill, J.T., Floss, C., Anand, M., Taylor, L.A., Nazarov, M.A., and Cohen, B.A. (2004) Petrogenesis of lunar highlands meteorites: Dhofar 025, Dhofar 081, Dar al Gani 262, and Dar al Gani 400. Meteoritics & planetary science, 39, 503–529.

Cheek, L. C., Donaldson Hanna, K. L., Pieters, C. M., Head, J. W., and Whitten, J. L. (2013) The distribution and purity of anorthosite across the Orientale basin: New perspectives from Moon Mineralogy Mapper data, Journal of Geophysical Research Planets, 118, 1805-1820.

Cheek, L.C., Pieters, C.M., Parman, S.W., Dyar, M.D., Speicher, E.A., and Cooper, R.F. (2011) Anorthite Synthesis Experiments with Application to Lunar Spectroscopy. 41st Lunar and Planetary Science Conference, 2438.

743 Cheek, L.C., Parman, S.W., and Pieters, C.M. (2010) Iron in Plagioclase: Synthesis Experiments
744 with Applications to Lunar Reflectance Spectroscopy. In AGU Fall Meeting Abstracts,
745 V21E-2370.
746 Cheek, L.C., and Pieters, C.M. (2014) Reflectance spectroscopy of plagioclase-dominated
747 mineral mixtures: Implications for characterizing lunar anorthosites remotely, American
748 Mineralogist, 99, 1871-1892.
749 Day J. M.D., Sossi, P.A., Shearer, CK., and Moynier, F. (2019) Volatile distributions in and on
750 the Moon revealed by Cu and Fe isotopes in the 'Rusty Rock' 66095. Geochimica et
751 Cosmochimica Acta, 266, 131-143.
752 Dohmen, R., and Blundy, J. (2014) A predictive thermodynamic model for element partitioning
753 between plagioclase and melt as a function of pressure, temperature and composition.
754 American Journal of science, 314, 1319–1372.
755 Donaldson, C.H., and Brown, R.W. (1977) Refractory megacrysts and magnesium-rich melt
756 inclusions within spinel in oceanic tholeiites: Indicators of magma mixing and parental
757 magma composition. Earth and Planetary Science Letters, 37, 81–89.
758 Donaldson Hanna, K.L., Bowles, N.E., Warren, T.J., Hamilton, V.E., Schrader, D.L., McCoy,
759 T.J., Temple, J., Clack, A., Calcutt, S., and Lauretta, D.S. (2021) Spectral
760 Characterization of Bennu Analogs Using PASCALE: A New Experimental Set-Up for
761 Simulating the Near-Surface Conditions of Airless Bodies. Journal of geophysical
762 research. Planets, 126, e2020JE006624.
763 Donaldson Hanna, K. L., Greenhagen, B. T., Patterson III, W. R., Pieters, C. M., Mustard, J. F.,
764 Bowles, N. E., Paige, D. A., Glotch, T. D., and Thompson, C. (2017) Effects of varying

765 environmental conditions on emissivity spectra of bulk lunar soils: Application to Diviner
766 thermal infrared observations of the Moon, Icarus, 283, 326-342.
767 Donaldson Hanna, K.L., Bowles, N., Greenhagen, B.T., Helbert, J., and Maturilli, A. (2018)
768 Spectral Characterization of a Suite of Well-Characterized Bulk Lunar Soils from the
769 Ultraviolet to the Far Infrared at the Planetary Emissivity Laboratory, DLR Berlin.
770 European Planetary Science Congress, 12, 712.
771 Donaldson Hanna, K.L., Wyatt, M.B., Thomas, I.R., Bowles, N.E., Greenhagen, B.T., Maturilli,
772 A., Helbert, J., and Paige, D.A. (2012) Thermal infrared emissivity measurements under a
773 simulated lunar environment: Application to the Diviner Lunar Radiometer Experiment.
774 Journal of Geophysical Research, 117, E00H05.
775 Donaldson Hanna, K.L., Cheek, L.C., Pieters, C.M., Mustard, J.F., Greenhagen, B.T., Thomas,
776 I.R., and Bowles, N.E. (2014) Global assessment of pure crystalline plagioclase across
777 the Moon and implications for the evolution of the primary crust. Journal of Geophysical
778 Research: Planets, 119, 1516–1545.
779 Dowty, E., Prinz, M., and Keil, K. (1974) Ferroan anorthosite: A widespread and distinctive
780 lunar rock type. Earth and Planetary Science Letters, 24, 15–25.
781 Drake, M.J., and Weill, D.F. (1975) Partition of Sr, Ba, Ca, Y, Eu^{2+}, Eu^{3+}, and other REE
782 between plagioclase feldspar and magmatic liquid: an experimental study. Geochimica et
783 Cosmochimica Acta, 39, 689–712.
784 Elardo, S.M., Shearer, C.K., and McCubbin, F.M. (2017) The role of KREEP in the production
785 of Mg-suite magmas and its influence on the extent of Mg-suite magmatism in the lunar
786 crust. 48th Lunar And Planetary Science Conference, JSC-CN-38651.

787 Elardo, S.M., Laneuville, M., McCubbin, F.M., and Shearer, C.K. (2020) Early crust building
788 enhanced on the Moon's nearside by mantle melting-point depression. Nature
789 Geoscience, 13, 339–343.
790 Falloon, T.J., and Crawford, A.J. (1991) The petrogenesis of high-calcium boninite lavas
791 dredged from the northern Tonga ridge. Earth and Planetary Science Letters, 102, 375–
792 394.
793 Fietzke, J., and Frische, M. (2016) Experimental evaluation of elemental behavior during LA-
794 ICP-MS: influences of plasma conditions and limits of plasma robustness. Journal of
795 Analytical Atomic Spectrometry, 31, 234–244.
796 Floss, C., James, O.B., McGee, J.J., and Crozaz, G. (1998) Lunar Ferroan Anorthosite
797 Petrogenesis: Clues from Trace Element Distributions in FAN Subgroups. Geochimica et
798 Cosmochimica Acta, 62, 1255–1283.
799 Foley, S., Tiepolo, M., and Vannucci, R. (2002) Growth of early continental crust controlled by
800 melting of amphibolite in subduction zones. Nature, 417, 837–840.
801 Gao, S., Liu, X., Yuan, H., Hattendorf, B., Günther, D., Chen, L., and Hu, S. (2002)
802 Determination of Forty Two Major and Trace Elements in USGS and NIST SRM Glasses
803 by Laser Ablation-Inductively Coupled Plasma-Mass Spectrometry. Geostandards and
804 Geoanalytical Research, 26, 181–196.
805 Greenhagen, B.T., Wagoner, C., Yasanayake, C.N., Donaldson Hanna, K., Bowles, N.E., and
806 Lucey, P.G. (2020) Thermal Infrared Spectra of Lunar Analog Mineral Mixtures Under
807 Simulated Airless Body Conditions and Comparison to LRO Diviner Observations.
808 American Geophysical Union, Fall Meeting 2020, P079-0016.
809 Grove, T.L., and Krawczynski, M.J. (2009) Lunar Mare Volcanism: Where Did the Magmas

Come From? Elements, 5, 29-34.

Günther, D., Frischknecht, R., Heinrich, C.A., and Kahlert, H.-J. (1997) Capabilities of an argon fluoride 193 nm excimer laser for laser ablation inductively coupled plasma mass spectometry microanalysis of geological materials. Journal of Analytical Atomic Spectrometry, 12, 939–944.

Heinrich, C.A., Pettke, T., Halter, W.E., Aigner-Torres, M., Audétat, A., Günther, D., Hattendorf, B., Bleiner, D., Guillong, M., and Horn, I. (2003) Quantitative multi-element analysis of minerals, fluid and melt inclusions by laser-ablation inductively-coupled-plasma mass-spectrometry. Geochimica et Cosmochimica Acta, 67, 3473–3497.

Herzberg, C., and Rudnick, R. (2012) Formation of cratonic lithosphere: An integrated thermal and petrological model. Lithos, 149, 4–15.

Hui, H., Guan, Y., Chen, Y., Peslier, A.H., Zhang, Y., Liu,Y., Flemming, R.L., Rossman, G.R., Eiler, J.M., Neal, C.R., and Osinski, G.R. (2017) A heterogeneous lunar interior for hydrogen isotopes as revealed by the lunar highlands samples. Earth and Planetary Science Letters, 473, 14–23.

Isshiki, N. (1958) Notes on Rock-Forming Minerals (3) Red coloration of anorthite from Hachijojima. The Journal of the Geological Society of Japan, 64, 644–647.

Kikuchi, Y. (1888). On anorthite from Miyakejima. The Journal of the College of Science, Imperial University of Tokyo, Japan, 2, 31-47.

Kimata, M., Nishida, N., Shimizu, M., Saito, S., Matsui, T., and Arakawa, Y. (1995) Anorthite megacrysts from island arc basalts. Mineralogical Magazine, 59(394), 1–14.

LaTourrette, T., and Wasserburg, G. J., (1998) Mg diffusion in anorthite: implications for the formation of early solar system planetesimals. Earth and Planetary Science Letters,

158(3-4), 91-108.

Lindsley D.H. (1969) Melting relations of plagioclase at high pressures, Origin of anorthosite and related rocks. New York State Museum and Science Service, 18, 39–46.

Lucey, P.G. (2002) Radiative transfer model constraints on the shock state of remotely sensed lunar anorthosites. Geophysical Research Letters, 29, 124-1-124-3.

Magna, T., Wiechert, U., and Halliday, A.N. (2006) New constraints on the lithium isotope compositions of the Moon and terrestrial planets. Earth and Planetary Science Letters, 243, 336–353.

May, T.W., and Wiedmeyer, R.H. (1998) A Table of Polyatomic Interferences in ICP-MS. Atomic Spectroscopy, 19, 150-155.

McDonough, W.F., and Sun, S. -s. (1995) The composition of the Earth. Chemical geology, 120, 223–253.

McGee, J.J. (1993) Lunar ferroan anorthosites: Mineralogy, compositional variations, and petrogenesis. Journal of Geophysical Research, 98, 9089–9105.

Milam, K.A. (2004) Accuracy of plagioclase compositions from laboratory and Mars spacecraft thermal emission spectra. Journal of Geophysical Research, 109, E04001.

Mosenfelder, J.L., Rossman, G.R., and Johnson, E.A. (2015) Hydrous species in feldspars: A reassessment based on FTIR and SIMS. American Mineralogist, 100, 1209–1221.

Murakami, H., Kimata, M., and Shimoda, S. (1991) Native copper included by anorthite from the island of Miyakejima: implications for arc magmatism. Journal of Mineralogy, Petrology and Economic Geology, 86, 364-374.

Nash, D.B., and Salisbury, J.W. (1991) Infrared reflectance spectra (2.2-15 μm) of plagioclase feldspars. Geophysical Research Letters, 18, 1151–1154.

Ohtake, M., Matsunaga, T., Haruyama, J. Yokota, Y., Morota, T., Honda, C., Ogawa, Y., Torii, M., Miyamoto, H., Arai, T., Hirata, N., Iwasaki, ., Nakamura, R., Hiroi, T., Sugihara, T., Takeda, H., Otake, H., Pieters, C. M., Saiki, K., Kitazato, K., Abe, M., Asada, N., Demura, H., Yamaguchi, Y., Sasaki, S., Kodama, S., Terazono, J., Shirao, M., Yamaji, A., Minami, S., Akiyama, H., and Josset, J.-L. (2009) The global distribution of pure anorthosite on the Moon, Nature, 461, 236-241.

Papike, J.J., Fowler, G.W., Shearer, C.K., and Layne, G.D. (1996) Ion microprobe investigation of plagioclase and orthopyroxene from lunar Mg-suite norites: Implications for calculating parental melt REE concentrations and for assessing postcrystallization REE redistribution. Geochimica et Cosmochimica Acta, 60, 3967–3978.

Papike, J.J., Fowler, G.W., and Shearer, C.K. (1997) Evolution of the lunar crust: SIMS study of plagioclase from ferroan anorthosites. Geochimica et Cosmochimica Acta, 61, 2343–2350.

Paton, C., Hellstrom, J., Paul, B., Woodhead, J., and Hergt, J. (2011) Iolite: Freeware for the visualisation and processing of mass spectrometric data. Journal of Analytical Atomic Spectrometry, 26, 2508–2518.

Pernet-Fisher, J.F., Joy, K.H., Martin, D.J.P. and Donaldson Hanna, K.L. (2017) Assessing the shock state of the lunar highlands: Implications for the petrogenesis and chronology of crustal anorthosites. Scientific Reports, 7, 5888.

Pernet-Fisher, J.F., Deloule, E., and Joy, K.H. (2019) Evidence of chemical heterogeneity within lunar anorthosite parental magmas. Geochimica et Cosmochimica Acta, 266, 109–130.

Pettke, T., Oberli, F., Audétat, A., Guillong, M., Simon, A.C., Hanley, J.J., and Klemm, L.M. (2012) Recent developments in element concentration and isotope ratio analysis of

879 individual fluid inclusions by laser ablation single and multiple collector ICP-MS. Ore
880 Geology Reviews, 44, 10–38.
881 Pouchou, J.-L., and Pichoir, F. (1991) Quantitative analysis of homogeneous or stratified
882 microvolumes applying the model “PAP.” In K.F.J. Heinrich and D.E. Newbury, Eds.,
883 Electron Probe Quantitation, p. 31–75. Springer US, Boston, MA.
884 Ramsey, M.S., and Christensen, P.R. (1998) Mineral abundance determination: Quantitative
885 deconvolution of thermal emission spectra. Journal of Geophysical Research: Solid Earth,
886 103(B1), 577-596.
887 Ruff, S.W., Christensen, P.R., Barbera, P.W., and Anderson, D.L. (1997) Quantitative thermal
888 emission spectroscopy of minerals: A laboratory technique for measurement and
889 calibration. Journal of Geophysical Research, 102, 14899–14913.
890 Salpas, P.A., Haskin, L.A., and McCallum, I.S. (1983) Stillwater Anorthosites: A lunar analog?
891 Journal of Geophysical Research, 88, B27–B39.
892 Shamloo, H.I., Till, C.B., and Hervig, R.L. (2021) Multi-mode magnesium diffusion in sanidine:
893 Applications for geospeedometry in magmatic systems. Geochimica et Cosmochimica
894 Acta, 298, 55–69.
895 Shearer, C.K., et al. (2006) Thermal and magmatic evolution of the Moon. Reviews in
896 Mineralogy and Geochemistry, 60, 365–518.
897 Shervais, J.W., and McGee, J.J. (1998) Ion and electron microprobe study of troctolites, norite,
898 and anorthosites from Apollo 14: evidence for urKREEP assimilation during petrogenesis
899 of Apollo 14 Mg-suite rocks. Geochimica et Cosmochimica Acta, 62, 3009–3023.

900 Shervais, J.W., and McGee, J.J. (1999) KREEP cumulates in the western lunar highlands; ion
901 and electron microprobe study of alkali-suite anorthosites and norites from Apollo 12 and
902 14. American Mineralogist, 84, 806–820.
903 Shimizu, N., and Hart, S.R. (1982) Applications of the ion microprobe to geochemistry and
904 cosmochemistry. Annual Review of Earth and Planetary Sciences, 10, 483-526.
905 Sisson, T.W., and Grove, T.L. (1993) Experimental investigations of the role of H_2O in calc-
906 alkaline differentiation and subduction zone magmatism. Contributions to Mineralogy
907 and Petrology, 113, 143–166.
908 Smith, J.V., Anderson, A.T., Newton, R.C., Olsen, E.J., and Wyllie, P.J. (1970) A petrologic
909 model for the moon based on petrogenesis, experimental petrology, and physical
910 properties. The Journal of Geology, 78, 381–405.Spudis, P.D., Hawke, B.R., and Lucey,
911 P. (1984) Composition of orientale basin deposits and implications for the lunar basin-
912 forming process. Journal of Geophysical Research, 89, C197.
913 Stakes, D.S., Shervais, J.W., and Hopson, C.A. (1984) The volcanic-tectonic cycle of the
914 FAMOUS and AMAR Valleys, Mid-Atlantic Ridge (36°47′N): Evidence from basalt
915 glass and phenocryst compositional variations for a steady state magma chamber beneath
916 the valley midsections, AMAR 3. Journal of Geophysical Research, 89, 6995–7028.
917 Sun, C., Graff, M., and Liang, Y. (2017) Trace element partitioning between plagioclase and
918 silicate melt: The importance of temperature and plagioclase composition, with
919 implications for terrestrial and lunar magmatism. Geochimica et Cosmochimica Acta,
920 206, 273–295.
921 Tepley, F.J., Lundstrom, C.C., McDonough, W.F., and Thompson, A. (2010) Trace element
922 partitioning between high-An plagioclase and basaltic to basaltic andesite melt at 1

923 atmosphere pressure. Lithos, 118, 82–94.

924 Thomas, I.R., Greenhagen, B.T., Bowles, N.E., Donaldson Hanna, K.L., Temple, J., and Calcutt,
925 S.B. (2012) A new experimental setup for making thermal emission measurements in a
926 simulated lunar environment. The Review of Scientific Instruments, 83, 124502.

927 Wang, H., Todd, T., Richter, D., and Simmons, G. Elastic properties of plagioclase aggregates
928 and seismic velocities in the moon. Proceedings of the Lunar Science Conference, 4,
929 2663.

930 Walker, D., and Hays, J.F. (1977) Plagioclase flotation and lunar crust formation. Geology,
931 Geophysics & Environment, 5, 425.

932 Walker, F., Lee, M., and Parsons, I. (1995). Micropores and micropermeable texture in alkali
933 feldspars: Geochemical and geophysical implications. Mineralogical Magazine, 59(396),
934 505-534.

935 Warren, P.H. (1985) The magma ocean concept and lunar evolution. Annual Review of Earth
936 and Planetary sciences, 13, 201–240.

937 Williams, J.P., Paige, D.A., Greenhagen, B.T., and Sefton-Nash, E. (2017) The global surface
938 temperatures of the Moon as measured by the Diviner Lunar Radiometer Experiment.
939 Icarus, 283, 300–325.

940 Wood, J.A., Dickey, J.S., Jr., Marvin, U.B., and Powell, B.N. (1970) Lunar anorthosites and a
941 geophysical model of the moon. Proceedings of the Apollo 11 Lunar Science Conference,
942 1, 965-988.

943 Woodhead, J.D., Hellstrom, J., Hergt, J. M., Greig, A., and Maas, R. (2007) Isotopic and
944 Elemental Imaging of Geological Materials by Laser Ablation Inductively Coupled
945 Plasma-Mass Spectrometry. Geostandards and Geoanalytical Research, 31, 331–343.

946 Xie, T., Osinski, G.R. and Shieh, S.R. (2021) Raman study of shock effects in lunar anorthite
947 from the Apollo missions. Meteoritics and Planetary Science, 56, 1633-1651.
948 Yurimoto, H., et al., (2011) Oxygen Isotopic Compositions of Asteroidal Materials Returned
949 from Itokawa by the Hayabusa Mission. Science, 333, 1116–1119.

950
951
952
953
954
955
956
957
958
959
960
961
962
963
964
965
966
967
968
969
970
971

972 Table 1. Dwell times in seconds of isotopes measured in the four LA-ICP-MS sessions. ^{44}Ca and
973 ^{139}La have been used as the internal standard for sessions I and II-IV respectively.
974

Session I		**Session I**		**Session II**		**Session III**		**Session IV**	
Mass	Dwell Times	Mass	Dwell Times	Mass	Dwell Times	Mass	Dwell Times	Mass	Dwell Times
^{44}Ca	0.01	^{141}Pr	0.01	^{139}La	0.01	^{139}La	0.01	^{139}La	0.01
^{49}Ti	0.015	^{146}Nd	0.01	^{147}Sm	0.12	^{175}Lu	0.4	^{169}Tm	0.3

This is the peer-reviewed, final accepted version for American Mineralogist, published by the Mineralogical Society of America.
The published version is subject to change. Cite as Authors (Year) Title. American Mineralogist, in press.
DOI: https://doi.org/10.2138/am-2023-9122. http://www.minsocam.org/

^{51}V	0.01	^{147}Sm	0.01	^{157}Gd	0.06	^{232}Th	0.1	^{174}Yb	0.3
^{52}Cr	0.01	^{153}Eu	0.01	^{159}Tb	0.02	^{238}U	0.01	^{175}Lu	0.3
^{55}Mn	0.01	^{157}Gd	0.01	^{163}Dy	0.06	$^{232}Th^{16}O$	0.01	^{232}Th	0.01
^{59}Co	0.01	^{159}Tb	0.01	^{165}Ho	0.02			^{238}U	0.01
^{63}Cu	0.01	^{163}Dy	0.01	^{166}Er	0.06			$^{232}Th^{16}O$	0.01
^{64}Zn	0.01	^{165}Ho	0.01	^{232}Th	0.01				
^{65}Cu	0.01	^{166}Er	0.01	^{238}U	0.01				
^{85}Rb	0.015	^{169}Tm	0.01	$^{232}Th^{16}O$	0.01				
^{88}Sr	0.015	^{174}Yb	0.01						
^{89}Y	0.01	^{175}Lu	0.01						
^{90}Zr	0.015	^{180}Hf	0.015						
^{93}Nb	0.01	^{208}Pb	0.01						
^{138}Ba	0.01	^{232}Th	0.01						
^{139}La	0.015	^{238}U	0.01						
^{140}Ce	0.010	$^{232}Th^{16}O$	0.01						

Table 2. Electron microprobe compositions in wt% of Miyake-jima anorthites cores and rims.

Sample	(n)	SiO_2	Al_2O_3	CaO	Na_2O	MgO	FeO	Total	An#
Core MG-1	22	43.68(16)	35.73(19)	19.41(10)	0.47(5)	0.08(1)	0.44(3)	99.8(26)	95.79(48)
Core MG-2	36	43.67(16)	35.5(16)	19.4(9)	0.52(6)	0.08(1)	0.46(3)	99.64(16)	95.4(51)

This is the peer-reviewed, final accepted version for American Mineralogist, published by the Mineralogical Society of America.
The published version is subject to change. Cite as Authors (Year) Title. American Mineralogist, in press.
DOI: https://doi.org/10.2138/am-2023-9122. http://www.minsocam.org/

Core MG-3	41	43.6(16)	35.77(17)	19.54(11)	0.43(9)	0.08(1)	0.42(3)	99.83(20)	96.09(54)
Core MG-4	33	43.75(20)	35.84(15)	19.42(9)	0.48(3)	0.08(1)	0.43(3)	100.01(27)	95.72(29)
Core MG-5	27	43.82(20)	35.61(17)	19.35(11)	0.54(5)	0.09(1)	0.45(3)	99.86(27)	95.22(43)
Core MG-6	68	43.76(13)	35.62(14)	19.4(8)	0.52(4)	0.08(2)	0.48(4)	99.85(21)	95.38(39)
Core MG-7	75	43.71(12)	35.63(14)	19.36(6)	0.5(10)	0.08(1)	0.46(4)	99.74(21)	95.39(42)
Rim MG-4	1	46.01	34.08	17.98	1.44	0.15	0.67	100.32	87.32
Rim MG-7	1	46.15	33.33	17.35	1.55	0.13	0.99	99.49	86.1

Anorthite (An#) has been calculated from 8 oxygen cation normalization. The wt% errors (in parentheses) are the one-sigma standard deviation from the mean with the least unit cited. Ti, Mn, Cr, P, and K measurements with the microprobe were consistently below detection limits of the individual elements and have not been reported. n is the number of analyses averaged for different grains' core domains.

Table 3. Trace element concentrations (in ppm) of Miyake-jima anorthites grain cores and rims from SIMS analyses. The errors are reported as one-sigma standard errors of the mean.

Sample	Li	Na	K	Ti
MG-1 core	0.2141(3)	3434.5(77)	44.94(2)	36.66(6)

This is the peer-reviewed, final accepted version for American Mineralogist, published by the Mineralogical Society of America.
The published version is subject to change. Cite as Authors (Year) Title. American Mineralogist, in press.
DOI: https://doi.org/10.2138/am-2023-9122. http://www.minsocam.org/

MG-1 rim	0.1216(4)	3065.04(58)	41.67(3)	33.54(5)
MG-2 core	0.2765(3)	3586.11(78)	46.31(6)	37.98(6)
MG-2 rim	0.3126(4)	3550.97(28)	60.95(8)	37.93(7)
MG-3 core	0.5099(6)	2997.38(55)	40.41(5)	33.37(5)
MG-3 rim	0.4343(5)	4655.57(112)	66.86(9)	35.77(5)
MG-4 core	0.752(7)	3652.3(133)	55.22(5)	36.72(7)
MG-4 rim	0.5018(5)	2921.05(89)	47.27(6)	32.82(6)
MG-5 core	0.1952(3)	3237.25(54)	42.9(6)	35.34(4)
MG-5 rim	0.1918(3)	3108.42(23)	37.69(2)	34.97(5)
MG-6 core	0.2451(6)	4424.55(107)	48.27(4)	42.81(6)
MG-6 rim	0.2042(6)	3664.27(92)	46.71(5)	37.11(7)
MG-7 core	0.1973(4)	3240.52(88)	37.98(2)	38.17(6)
MG-7 rim	0.6952(6)	5525.25(175)	90.3(4)	47.16(6)

Table 4. LA-ICP-MS trace element composition in ppm of average Miyake-jima anorthite cores and single raster analyses of the rims in MG-4 and MG-7.

	MG-1 core	MG-2 core	MG-3 core	MG-4 core	MG-5 core	MG-6 core	MG-7 core	MG-4 rim	MG-7 rim
Ti	38.8(33)	49.9(151)	37.4(32)	66.0(25)	45.0(23)	45.4(21)	43.0(19)	375.1(70)	43.5(11)
V	1.12(9)	1.31(83)	1.09(8)	0.94(3)	1.04(6)	1.20(6)	1.12(6)	8.03(21)	1.13(5)
Cr	0.71(9)	0.73(56)	0.73(27)	0.53(6)	0.58(14)	0.71(11)	0.67(19)	4.42(73)	0.69(10)

This is the peer-reviewed, final accepted version for American Mineralogist, published by the Mineralogical Society of America.
The published version is subject to change. Cite as Authors (Year) Title. American Mineralogist, in press.
DOI: https://doi.org/10.2138/am-2023-9122. http://www.minsocam.org/

Mn	22.7(4)	23.7(31)	22.8(4)	21.2(4)	22.3(3)	24.1(36)	22.4(10)	183.2(13)	32.9(4)
Co	0.32(4)	0.32(7)	0.33(4)	0.29(2)	0.33(4)	0.31(3)	0.32(3)	2.45(15)	0.26(2)
Cu^{63}	1.00(19)	0.95(15)	2.16(86)	2.02(44)	1.00(9)	1.15(36)	1.21(36)	10.27(38)	2.49(9)
Zn	1.24(15)	1.36(31)	1.22(27)	1.00(9)	1.31(9)	1.36(13)	1.26(14)	9.00(53)	1.51(11)
Cu^{65}	0.90(18)	1.45(207)	2.08(89)	2.08(41)	0.97(13)	1.14(34)	1.19(39)	10.6(7)	2.56(13)
Ba	5.45(21)	5.99(34)	5.18(32)	5.14(13)	5.76(24)	5.80(19)	5.50(13)	2806(14)	299.4(22)
Sr	309.1(35)	326.2(62)	310.9(97)	319.8(25)	325.4(44)	320.3(39)	323.3(43)	0.3(1)	0.06(1)
Nd	0.05(1)	0.06(2)	0.06(1)	0.05(1)	0.06(1)	0.05(1)	0.06(1)	44.14(49)	6.26(9)
La	0.027(3)	0.033(6)	0.028(4)	0.030(3)	0.033(5)	0.032(4)	0.031(4)	0.270(3)	0.030(1)
Ce	0.06(1)	0.07(1)	0.06(1)	0.06(1)	0.07(1)	0.07(1)	0.06(1)	0.51(4)	0.08(1)
Pr	0.010(2)	0.011(3)	0.011(3)	0.010(1)	0.011(2)	0.011(2)	0.011(3)	0.093(17)	0.009(2)
Nd	0.05(1)	0.06(2)	0.06(1)	0.05(1)	0.06(1)	0.05(1)	0.06(1)	0.48(9)	0.08(2)
Sm*	0.011(2)	0.012(1)	0.015(2)	0.015(2)	0.011	0.015(1)	0.013(2)	<d.l.	<d.l.
Eu	0.064(10)	0.068(7)	0.057(13)	0.062(7)	0.069(5)	0.063(7)	0.063(7)	0.550(5)	0.070(1)
Gd*	0.0105(0)	0.0108(8)	0.0147(20)	0.0128(14)	0.0095	0.0135(14)	0.0123(24)	<d.l.	<d.l.
Tb*	0.0020(2)	0.0013(2)	0.0016(2)	0.0018(4)	0.0014	0.0017(2)	0.0015(4)	<d.l.	<d.l.
Dy*	0.0086(34)	0.0068(4)	0.0097(12)	0.0082(13)	0.0050	0.0089(9)	0.0079(14)	<d.l.	<d.l.
Ho*	0.0015(11)	0.0012(1)	0.0016(3)	0.0015(3)	0.0010	0.0014(2)	0.0014(4)	<d.l.	<d.l.
Er*	0.0036(21)	0.0026(3)	0.0035(6)	0.0031(9)	0.0027	0.0033(5)	0.0030(9)	<d.l.	<d.l.
Tm*	0.00034(16)	0.00029(4)	0.00027(4)	0.00030(8)	0.00031	0.00029(3)	0.00029(6)	<d.l.	<d.l.
Yb*	0.0020(6)	0.0018(3)	0.0016(3)	0.0016(2)	0.0020	0.0017(2)	0.0017(3)	<d.l.	<d.l.
Lu*	0.00019(6)	0.00020(4)	0.00018(5)	0.00018(2)	0.00022(9)	0.00020(3)	0.00019(2)	<d.l.	<d.l.
Y	0.036(8)	0.055(47)	0.038(13)	0.039(4)	0.038(8)	0.042(9)	0.038(7)	<d.l.	<d.l.
Pb	0.08(3)	0.06(1)	0.19(6)	0.05(1)	0.06(2)	0.09(3)	0.10(6)	<d.l.	0.30(5)

The errors reported for the cores and rims are the one-sigma standard errors of all the individual analyses averaged for each sample.
* Elements for which La was used as the internal standard in sessions II - IV.
<d.l. indicates analyses that were below the detection limits.
Data points where uncertainties are not mentioned are single raster analyses for that sample. Number of data points averaged and individual analyses for each crystal have been reported in the Supplementary Table S2.

Table 5. 1-sigma percent standard deviations of individual LREEs in the Miyake-jima crystal cores.

Sample	# of analyses	La	Ce	Pr	Nd	Eu
MG-1	7	11.45	10.30	17.02	22.09	15.82
MG-2	28	17.45	22.17	30.91	25.04	9.88
MG-3	13	16.12	18.15	24.08	23.83	23.43

This is the peer-reviewed, final accepted version for American Mineralogist, published by the Mineralogical Society of America.
The published version is subject to change. Cite as Authors (Year) Title. American Mineralogist, in press.
DOI: https://doi.org/10.2138/am-2023-9122. http://www.minsocam.org/

MG-4	13	9.70	8.65	11.50	19.98	10.98
MG-5	9	13.99	6.16	20.97	23.79	6.75
MG-6	23	13.55	8.63	17.56	22.60	11.36
MG-7	32	13.22	11.69	26.78	23.34	11.63

Table 6. Major, minor, and trace element concentrations of Miyake-jima anorthites grain cores from a combination of data collected from microprobe, SIMS, and LA-ICPMS analyses.

Major and minor elements

SiO_2	(wt%)	43.71(6)	Si	(wt%)	20.43(3)
Al_2O_3	(wt%)	35.67(13)	Al	(wt%)	18.88(7)

This is the peer-reviewed, final accepted version for American Mineralogist, published by the Mineralogical Society of America.
The published version is subject to change. Cite as Authors (Year) Title. American Mineralogist, in press.
DOI: https://doi.org/10.2138/am-2023-9122. http://www.minsocam.org/

CaO	(wt%)	19.41(6)	Ca	(wt%)	13.87(4)
Na_2O	(wt%)	0.50(3)	Na	(wt%)	0.36(3)
MgO	(wt%)	0.08(1)	Mg	(wt%)	0.048(6)
FeO	(wt%)	0.45(2)	Fe	(wt%)	0.35(2)

Trace elements

K	(ppm)	44.0(38)	Mn	(ppm)	22.77(97)
Ti	(ppm)	46.5(96)	Sr	(ppm)	319.3(68)
Ba	(ppm)	5.55(32)	Sm	(ppm)	0.013(2)
Li	(ppm)	0.32(14)	Eu	(ppm)	0.064(4)
V	(ppm)	1.12(12)	Gd	(ppm)	0.012(2)
Cr	(ppm)	0.67(8)	Tb	(ppm)	0.0016(2)
Co	(ppm)	0.32(1)	Dy	(ppm)	0.008(2)
Cu^{63}	(ppm)	1.43(48)	Ho	(ppm)	0.0014(2)
Zn	(ppm)	1.25(12)	Er	(ppm)	0.0031(4)
Cu^{65}	(ppm)	1.40(50)	Tm	(ppm)	0.0003(2)
Nd	(ppm)	0.06(1)	Yb	(ppm)	0.0018(2)
La	(ppm)	0.031(2)	Lu	(ppm)	0.00019(1)
Ce	(ppm)	0.06(1)	Y	(ppm)	0.04(1)
Pr	(ppm)	0.011(5)	Pb	(ppm)	0.09(5)
Nd	(ppm)	0.06(1)			

The errors are reported as one-sigma standard errors of the mean (e.g. 43.71 +/- 0.06 wt.% is represented as 43.71(6)).

Figure Captions

Figure 1. Miyake-jima anorthite megacrysts. On the left are the intact megacrysts highlighting their basaltic coating. On the right are crushed megacrysts showing the clear crystal cores of the sample.

1099

1100 Figure 2. Back scattered electron (BSE) images of Miyake-jima Grains (MG-1 — 7). The
1101 microprobe compositional variation between anorthite (An) - albite (Ab) and major elements
1102 (SiO_2, Al_2O_3, FeO, and MgO) are shown across the profile marked (as Rim-L to Rim-R) in the
1103 corresponding BSE images. 1-sigma standard deviations of mean anorthite concentration have
1104 been reported for the cores of each crystal fragment.

1105

1106 Figure 3. Variation in Li, K, Ti, and Na (ppm) as measured by individual SIMS spot analyses.
1107 Pairs of cores (black-bars) and rims (white-bars) from the same Miyake-jima crystal indicate the
1108 intra-granular chemical variability in Li, K, Na, and Ti. 1-σ standard errors from individual
1109 SIMS analytical spots are shown as gray bars. The average and 1-σ standard deviation of
1110 population of the core is depicted by the shaded region. Note that only MG-4 and MG-7 sample
1111 the albitic rim, while other crystals show heterogeneity in the core.

1112

1113 Figure 4. Chondrite-normalized (McDonough and Sun 1995) individual LREEs across profiles of
1114 crystals MG-4 and MG-7, where the distance on the x-axes represent scan steps from edge to
1115 edge of individual crystals. The corresponding BSE images show the pits formed due to ablation.
1116 These raster profiles have been reconstructed using data from 'Session I' where laser spot size of
1117 35 μm were used to ablate raster lines of ~75 μm length.

1118

1119 Figure 5. (Left) NIR reflectance spectrum of Miyake-jima anorthite (particle size fraction 125 –
1120 250 μm) with the characteristic 1.25 μm band for crystalline plagioclase. (Right) TIR emissivity

1121 spectra of Miyake-jima anorthite (particle size fraction < 25 μm) measured under ambient and
1122 simulated lunar environment (SLE) conditions.
1123
1124 Figure 6. Average anorthite content (An#, calculated from 8 oxygen formula units) of the
1125 individual Miyake-jima grain cores with 1-σ standard errors from the mean and single rim
1126 analyses from MG-4 and MG-7. The average anorthite content of the 7 individual grains
1127 analyzed in this study is $An_{95.5 \pm 0.3}$ (1-σ) represented by the shaded area.
1128
1129 Figure 7. (a-g) Average chondrite-normalized (McDonough and Sun 1995) REE patterns of the
1130 seven individual Miyake-jima crystals with their 1-sigma standard deviation (blue bars)
1131 calculated from each individual line analyses made for different Miyake-jima grains, and (h) the
1132 number of analyses (above detection limit) used in the construction of the REE patterns.
1133
1134 Figure 8. Anorthite content versus (a) FeO and (b) MgO wt% (from electron microprobe) for
1135 Miyake-jima cores and rims compared to lunar ferroan anorthosites (FAN). Gray error bars show
1136 1-sigma standard error on major element and anorthite concentrations. FAN major element
1137 composition is based on Papike et al. (1997) and McGee (1993) that include a compilation of
1138 analyses performed on lunar FAN plagioclase from samples 60025, 15415, 60015, 60055,
1139 60215, 61016, 62255, 64425, 64435, 65035, 65315, 67525, 67535, 67536, 68515, and 69955.
1140
1141 Figure 9. Comparison of CI-normalized REE concentrations of Miyake-jima anorthites and lunar
1142 plagioclase grains (compiled by Cahill et al., 2004). REE concentrations of FAN (ferroan
1143 anorthosite), HMS (high-magnesium suite), and HAS (high alkali suite) were compiled from

literature Floss et al., (1998); Papike et al., (1997); Papike et al., (1996); Shervais and McGee (1998); Shervais and McGee (1999).

Figure 10. Average primitive mantle-normalized (McDonough and Sun, 1995) spidergrams of the seven individual Miyake-jima crystals. Li and K values are collected from SIMS while other trace elements are from LA-ICP-MS analyses. The gray field shows trace element concentrations of the lunar anorthosite suites from the literature. Li data for FAN represents solution LA-ICP-MS measurements from 62255 and 65315 reported by Magna et al., 2006. Other FAN trace elements were measured by LA-ICP-MS of plagioclase mineral separates of 15415, Apollo 16 return samples (Pernet-Fisher et al., 2019) and also includes the REE compilation done by Cahill et al., 2004. Data points identified as outliers with respect to the majority of the samples have been marked as points (grey squares).

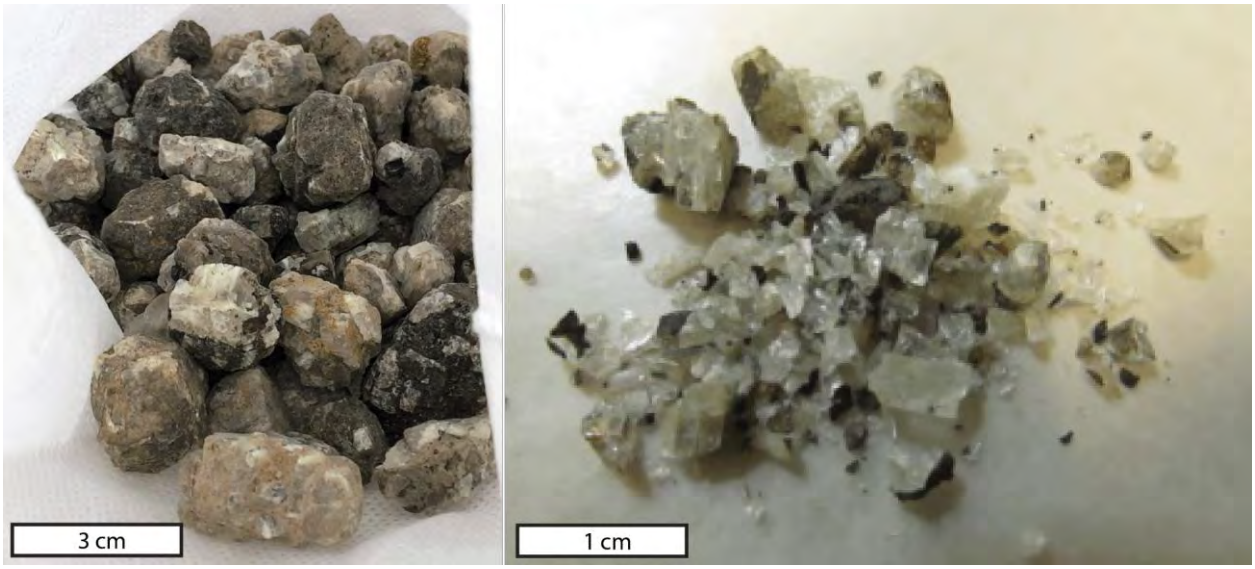

Figure 1.

1163
1164
1165
1166
1167
1168
1169
1170
1171
1172
1173
1174
1175

This is the peer-reviewed, final accepted version for American Mineralogist, published by the Mineralogical Society of America.
The published version is subject to change. Cite as Authors (Year) Title. American Mineralogist, in press.
DOI: https://doi.org/10.2138/am-2023-9122. http://www.minsocam.org/

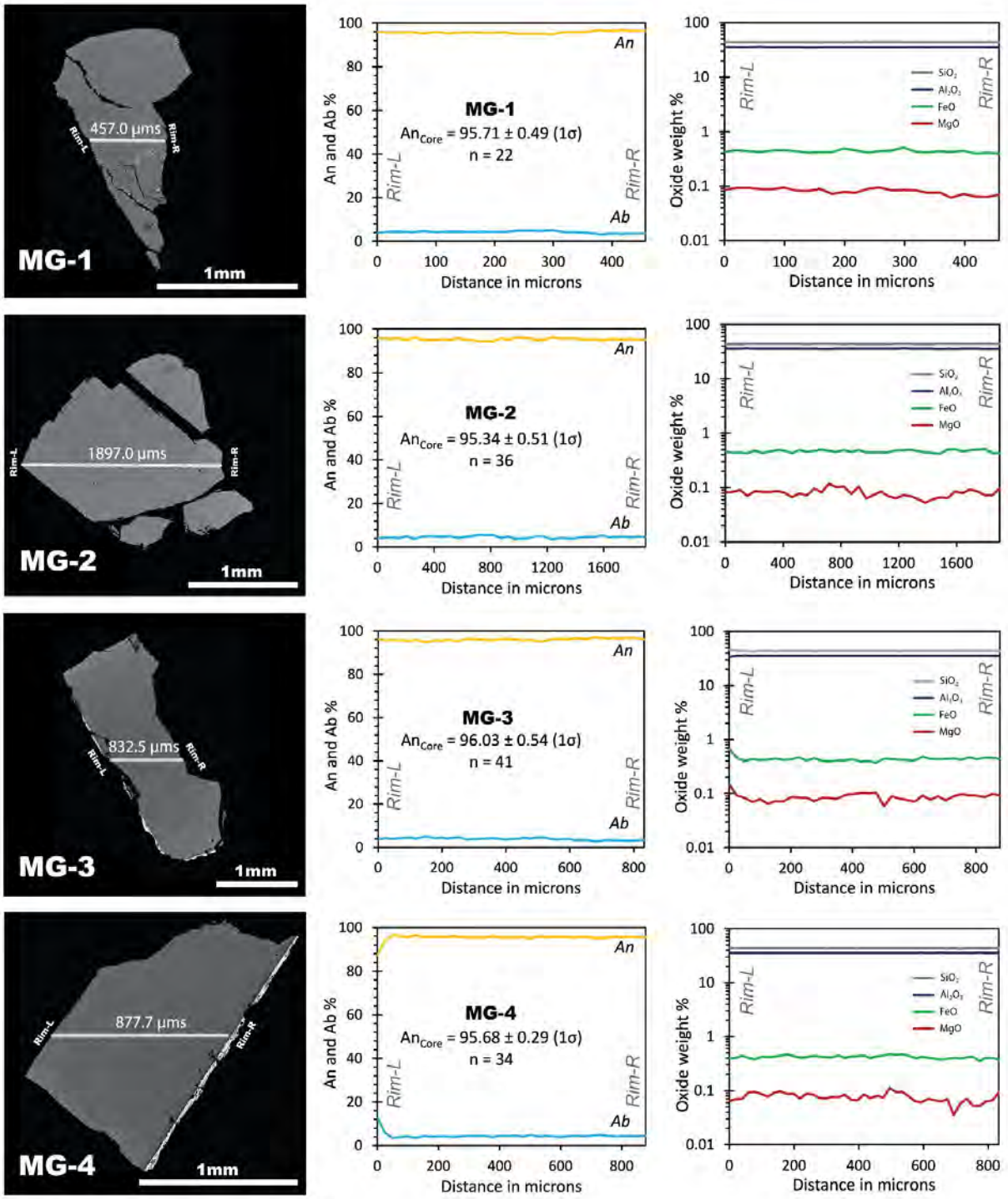

Figure 2.

This is the peer-reviewed, final accepted version for American Mineralogist, published by the Mineralogical Society of America.
The published version is subject to change. Cite as Authors (Year) Title. American Mineralogist, in press.
DOI: https://doi.org/10.2138/am-2023-9122. http://www.minsocam.org/

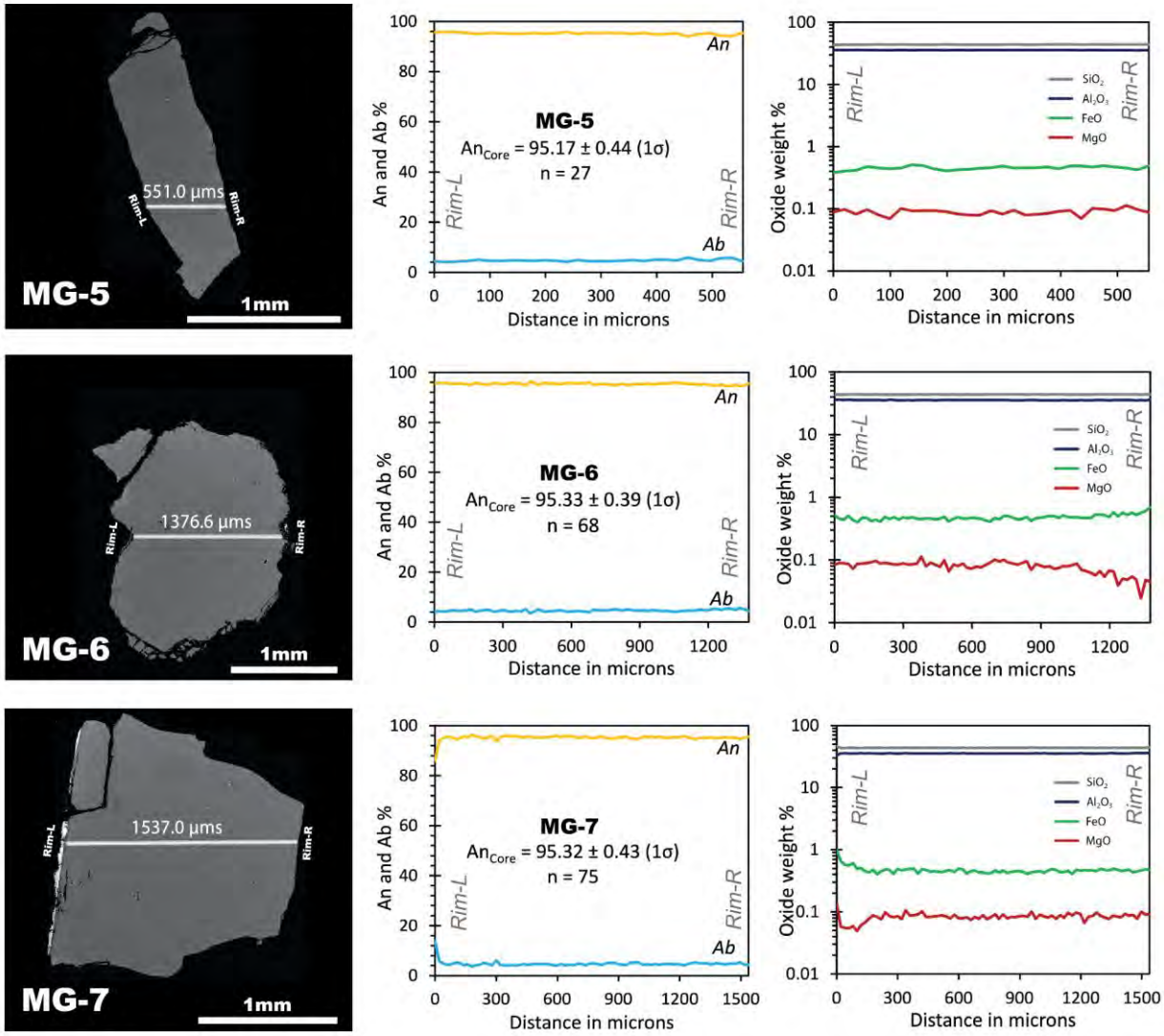

Figure 2. (continued)

This is the peer-reviewed, final accepted version for American Mineralogist, published by the Mineralogical Society of America.
The published version is subject to change. Cite as Authors (Year) Title. American Mineralogist, in press.
DOI: https://doi.org/10.2138/am-2023-9122. http://www.minsocam.org/

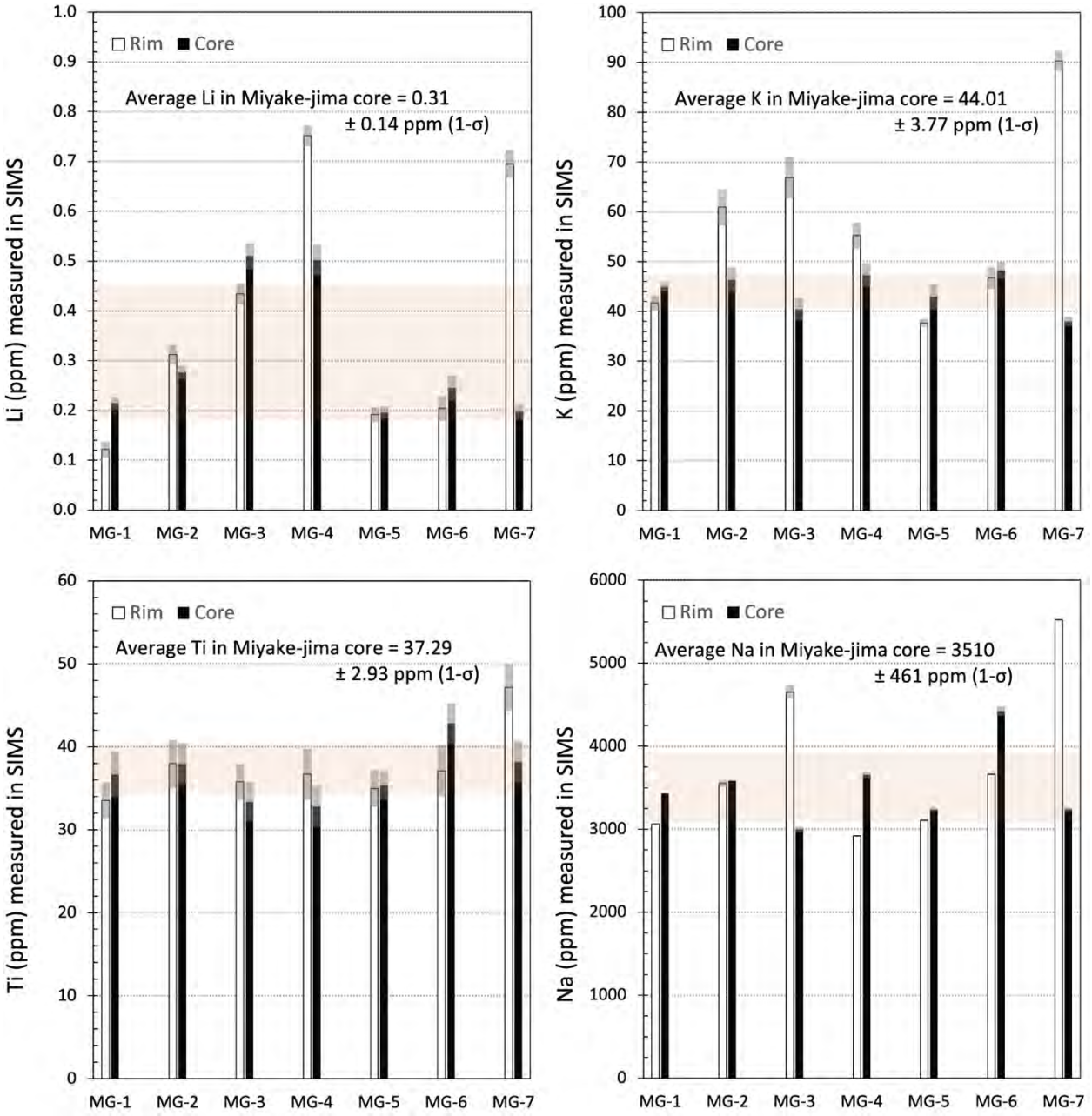

Figure 3.

This is the peer-reviewed, final accepted version for American Mineralogist, published by the Mineralogical Society of America.
The published version is subject to change. Cite as Authors (Year) Title. American Mineralogist, in press.
DOI: https://doi.org/10.2138/am-2023-9122. http://www.minsocam.org/

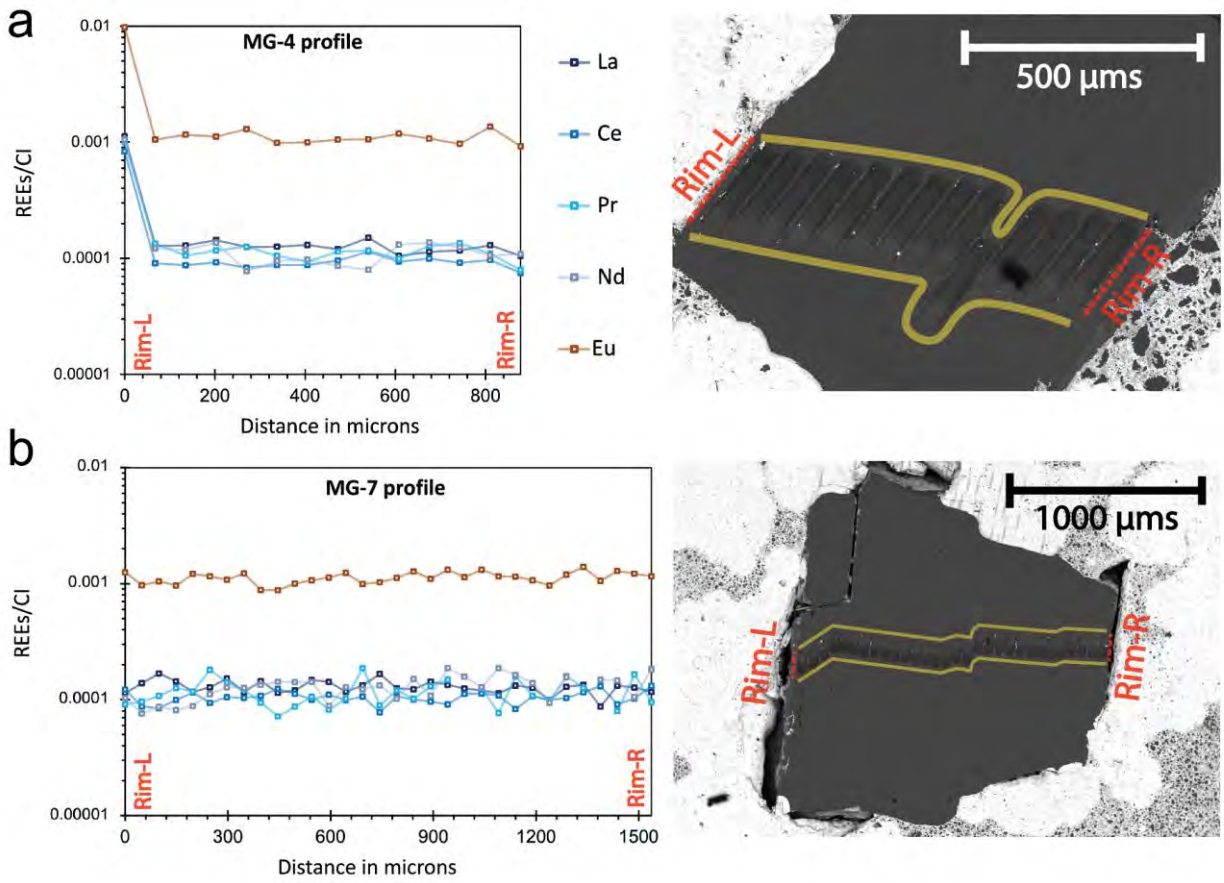

Figure 4.

This is the peer-reviewed, final accepted version for American Mineralogist, published by the Mineralogical Society of America.
The published version is subject to change. Cite as Authors (Year) Title. American Mineralogist, in press.
DOI: https://doi.org/10.2138/am-2023-9122. http://www.minsocam.org/

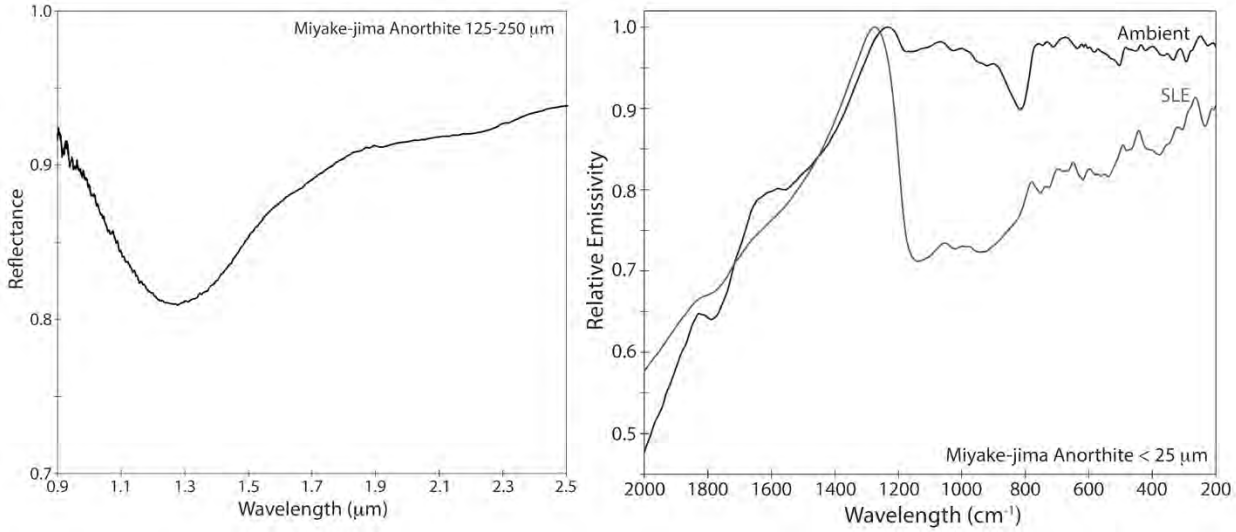

Figure 5.

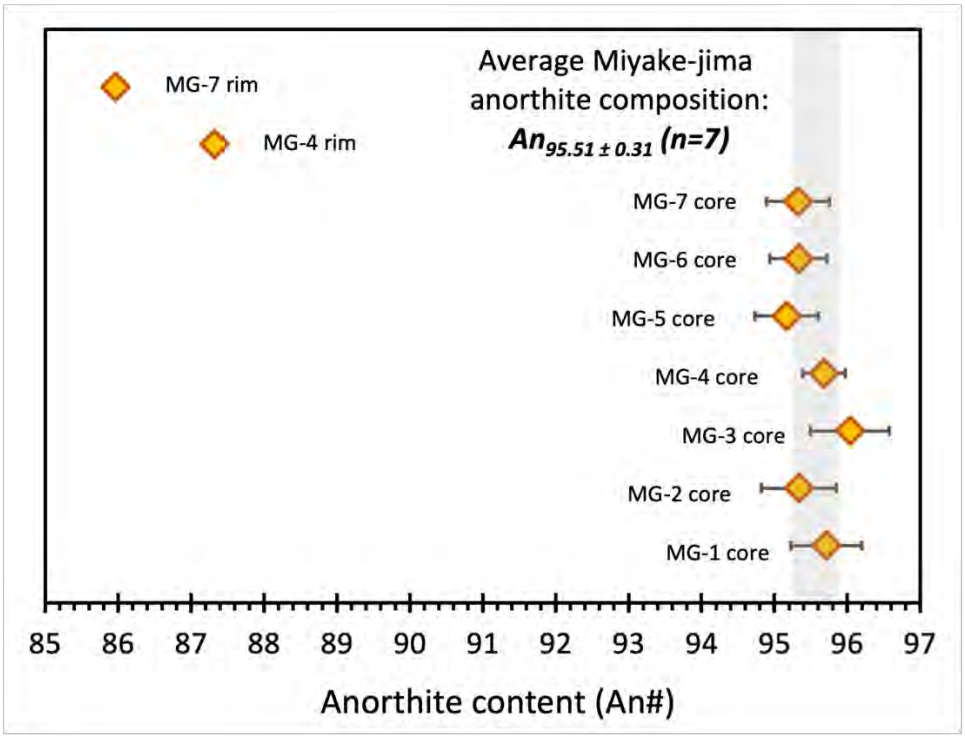

Figure 6.

This is the peer-reviewed, final accepted version for American Mineralogist, published by the Mineralogical Society of America.
The published version is subject to change. Cite as Authors (Year) Title. American Mineralogist, in press.
DOI: https://doi.org/10.2138/am-2023-9122. http://www.minsocam.org/

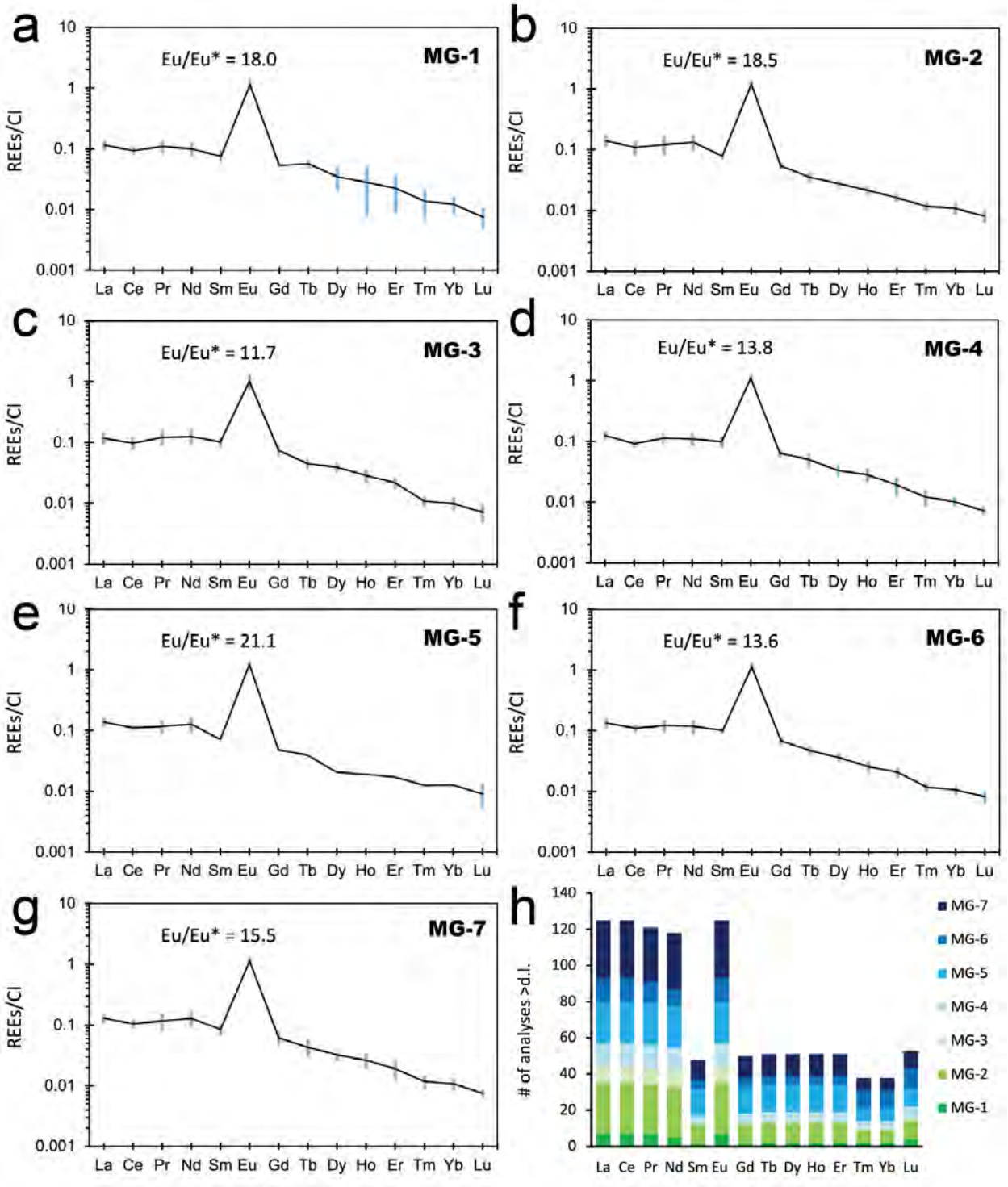

Figure 7.

This is the peer-reviewed, final accepted version for American Mineralogist, published by the Mineralogical Society of America.
The published version is subject to change. Cite as Authors (Year) Title. American Mineralogist, in press.
DOI: https://doi.org/10.2138/am-2023-9122. http://www.minsocam.org/

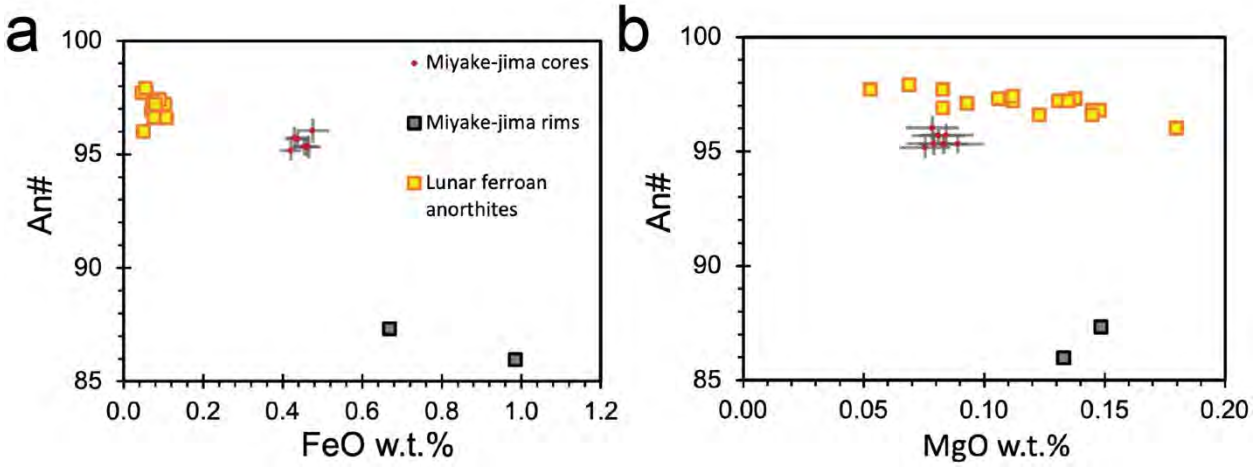

Figure 8.

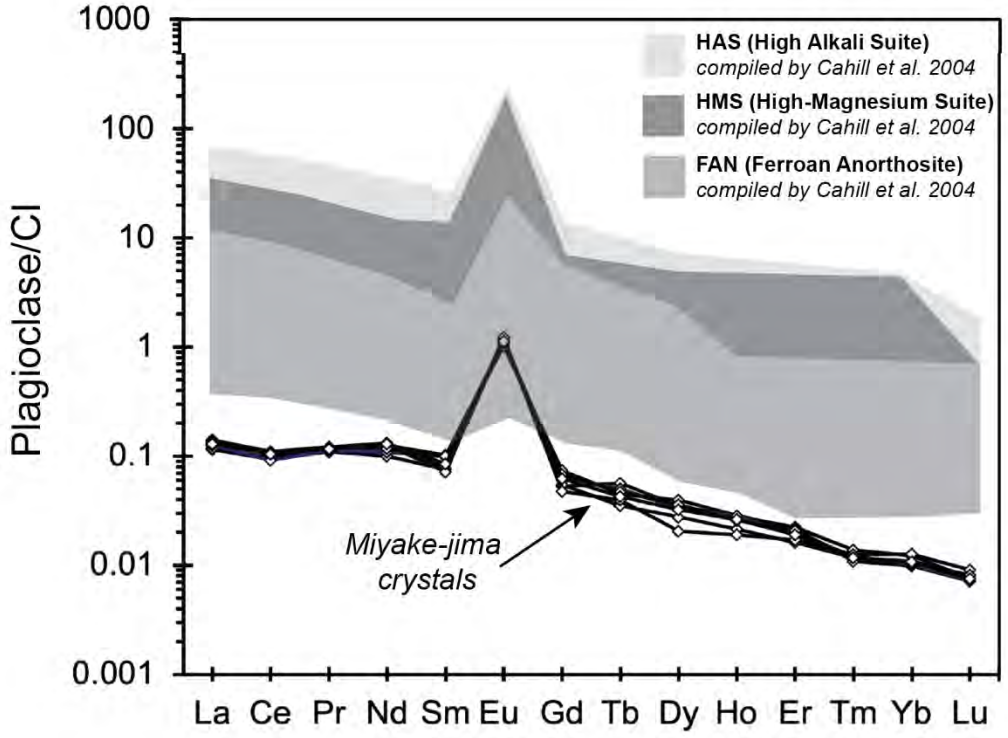

Figure 9.

.

This is the peer-reviewed, final accepted version for American Mineralogist, published by the Mineralogical Society of America.
The published version is subject to change. Cite as Authors (Year) Title. American Mineralogist, in press.
DOI: https://doi.org/10.2138/am-2023-9122. http://www.minsocam.org/

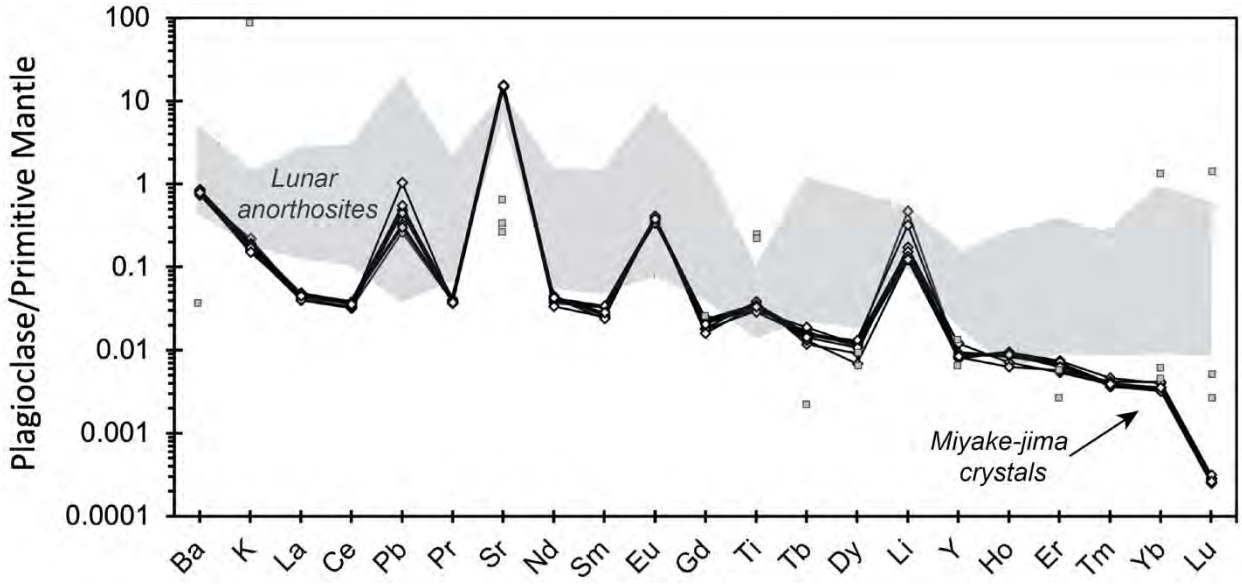

Figure 10.